



TECHNISCHE
UNIVERSITÄT
WIEN

Vienna University of Technology

DIPLOMARBEIT

Implementation of Tavis Cummings model for the study of coherent information transfer between NV spin ensembles

*ausgeführt am Atominstitut der Technischen Universität Wien
unter der Anleitung von*

Univ. Prof. Dr. Hannes-Jörg Schmiedmayer

Univ. Ass. Dr. Johannes Majer

*eingereicht an der
Technischen Universität Wien
Fakultät für Physik
von*

Stefan Nevlacsil

Matrikelnummer: 0925413

Antonie-Alt-Gasse 4/5/49, 1100 Wien

Wien, am 26. 10. 2015

Abstract

Utilizing quantum mechanics for information processing has certain limits depending on the physical properties used. Desirable are systems with long coherence and short operation times which are versatile in production. Promising candidates for information processing units, the qubits, use electron spins or superconducting properties. Electron spins show long coherence times, however, are affected by slow operation times due to their weak coupling to external fields. This makes them suitable for information storage purposes. On the other hand, superconducting (SC) qubits, based on Josephson Junctions, can be utilized for information processing as they show fast operation despite their short coherence times. They have the additional advantage that they have flexible tuning properties and can be scaled easier as their limit is mainly in fabrication. In hybrid quantum systems different qubit types are connected via a quantum bus to combine advantages and counteract the disadvantages of each system. With the quantum bus the information is transferred between the quantum operation unit, the SC qubits, and quantum storage, the electron spin qubits.

This thesis examines the feasibility of coherent information transfer between quantum storages along a quantum bus. For this case an ensemble of electron spins is used to increase the effective coupling to external fields by the root of the electron spin number. This leads to a better signal to noise ratio with the downside of decreased coherence times in the experimental setup. The spin ensemble is implemented using Nitrogen Vacancy (NV) defects in diamond. For the experiment two diamonds are placed on a microwave resonator, which acts as the quantum bus. A probe field is applied to the resonator and the transmission spectrum is influenced by Zeeman tuning the transition frequency of the spins in and out of resonance.

The proof of coherent coupling between the spatially separated diamonds is given in two ways. Firstly the typical root increase of coupling strength for ensembles with the overlap of both diamond transition frequencies. This is measured directly with the spin transitions on resonance with the resonator producing an avoided crossing, which is proportional to the coupling strength. Secondly a theoretical model for the transmission spectrum is implemented on basis of the interaction of spin ensembles with electromagnetic fields, described by the Tavis Cummings Hamiltonian. The steps of parameter determination and calculation of the spectrum is shown in this work. Comparison between measurement and calculation shows the same behaviour, confirming the assumed coherent coupling of the two ensembles through the quantum bus.

In the outlook a different type of spin ensemble in the form of nanomagnets is briefly discussed. They can be chemically altered and are therefore not as limited in their properties.

Zusammenfassung

Die Anwendung von Quantenmechanik für die Informationstechnologie ist begrenzt durch die Wahl der verwendeten physikalischen Eigenschaft. Vorteilhaft sind Systeme veränderbar in der Produktion mit langen Kohärenz- und kurzen Operationszeiten. Vielversprechend sind dabei Informationsträger, die Qubits, die auf Elektronenspins oder supraleitenden Eigenschaften basieren. Elektronenspins zeigen lange Kohärenzzeiten sind allerdings durch ihre schwache Kopplung an externe Felder von langsamen Operationszeiten betroffen. Mit diesen Eigenschaften eignen sie sich für Informationsspeicherung. Auf der anderen Seite sind Supraleitende (SC) Qubits, basierend auf Josephsonkontakten, besser geeignet für Informationsverarbeitung, da sie schnelle Operationszeiten besitzen trotz des Nachteils von kurzen Kohärenzzeiten. Ein weiterer Vorteil von SC Qubits ist, dass sie vielseitig herstellbar sind, da sie nur durch Fabrikation limitiert sind. In hybriden Quantensystemen werden unterschiedliche Qubit Arten verbunden durch einen Quantenbus, wodurch deren Vorteile kombiniert und die Nachteile ausgeglichen werden. Der Quantenbus transferiert die Information zwischen der Quantenoperationseinheit, den SC Qubits, und dem Quantenspeicher, den Elektronenspin Qubits.

Diese Arbeit befasst sich mit der Möglichkeit von kohärentem Informationstransfer zwischen Quantenspeicher durch den Quantenbus. Zu diesem Zweck wird ein Ensemble von Elektronenspins verwendet, bei dem die effektive Kopplungsstärke zu einem externen Feld durch einen Faktor verstärkt wird, der der Wurzel der Anzahl der Elektronenspins entspricht. Dadurch entsteht ein besseres Signal-Rausch-Verhältnis mit dem Nachteil von reduzierten Kohärenzzeiten im Experiment. Das Spinensemble setzt sich zusammen aus Stickstoff-Fehlstellen-Zentren in einem Diamant. Im Experiment liegen zwei Diamanten auf einem Mikrowellenresonator, der als Quantenbus agiert. Beim Anlegen eines Feldes durch den Resonator wird ein Transmissionsspektrum gemessen, durch Zeemann Verschiebung der Spin Übergangsfrequenzen zu der Resonatorfrequenz wird dieses verändert.

Der Beweis für kohärentes Koppeln der räumlich getrennten Diamanten wird auf zwei Arten erbracht. Einerseits über das typische Wurzel Verhalten der Kopplungsstärke von Ensembles beim Überlagern der beiden Übergangsfrequenzen der Diamanten. Dieses Verhalten wird direkt gemessen, da bei Übereinstimmung beider Übergangsfrequenzen mit der Resonanzfrequenz die Frequenzen proportional zu der Kopplungsstärke aufsplitten. Andererseits wird eine theoretisches Model implementiert für die Berechnung des Transmissionsspektrums, basierend auf der Interaktion eines Spinensembles mit dem elektromagnetischen Feld, die von einem Tavis Cummings Hamiltonian beschrieben wird.

Die Schritte der Parameterbestimmung und Berechnung des Spektrums werden in dieser Arbeit gezeigt. Vergleiche der Messung mit der Berechnung zeigen das gleiche Verhalten, wodurch die angenommene kohärente Kopplung zwischen der zwei Ensembles durch den Quantenbus bestätigt wird.

Im letzten Kapitel wird kurz ein anderer Typ von Ensemble beschrieben, der auf Nanomagneten basiert. Diese können chemisch verändert werden und sie dadurch in ihren Eigenschaften nicht so stark limitiert.

Contents

Abstract	i
Zusammenfassung	ii
Contents	iv
List of Figures	vi
1 Introduction	1
2 Theory	3
2.1 Spin-Field Interaction	3
2.1.1 Tavis Cummings Model	3
2.1.2 Solution of Tavis Cummings	6
2.1.3 Resonant Regime	9
2.1.4 Dispersive Regime	11
2.2 Spin System NV^-	11
2.2.1 Electronic Ground State	12
2.2.2 Defect Reference Frame	14
2.3 Cavity	16
2.3.1 Basic Principle of Microwave Resonators	16
2.3.2 $\lambda/2$ Resonator	19
2.3.3 Lumped Element Resonator (LER)	19
2.4 Implementation of Tavis Cummings	20
2.4.1 Measurement Requirements	21
3 Measurement Setup	23
3.1 Adiabatic Demagnetization Refrigerator (ADR)	23
3.2 Vector Network Analyzer (VNA)	25
3.3 Microwave Generator (MG)	27
3.4 Resonators	27
4 Measurements and Results	28
4.1 Basic Parameters and Optimization	28
4.2 Coherent Coupling of Two Ensembles	35
5 Outlook	43

5.1 Alternative Spin Ensemble: Nanomagnets	43
Bibliography	48
Acknowledgements	48

List of Figures

2.1	Experimental setup	7
2.2	Tavis Cummings eigenvalues for strong coupling	10
2.3	Tavis Cummings eigenvalues for weak coupling	10
2.4	Nitrogen Vacancy (NV) crystal structure	12
2.5	NV eigenvalues tuned by a magnetic field in z direction	14
2.6	Projection of 4 NV directions to the (001) plane	15
2.7	Transition frequencies of 4 NV subensembles for in plane fields	16
2.8	Lumped LCR circuit schematic	17
2.9	Lumped LCR spectrum	17
2.10	Coplanar wave guide structure	19
3.1	Measurement setup	24
3.2	Helmholtz coils setup	25
3.3	Resonator box	27
4.1	Temperature dependency of resonance frequency f_{res} and quality factor Q	29
4.2	Zero field splitting Berkeley sample	30
4.3	Spectroscopic measurement for the magnetic field angles ($\phi = 0^\circ, \theta = 90^\circ$)	31
4.4	θ offset measurement	32
4.5	ϕ offset/avoided crossing field amplitude measurement	32
4.6	Spectroscopic measurement with corrected angles ($\phi = 2.46^\circ, \theta = 90.76^\circ$)	33
4.7	Transmission amplitude at avoided crossing	33
4.8	Theory/measurement comparison of avoided crossing	34
4.9	Calculated spectroscopic measurement ($\phi = 2.46^\circ, \theta = 90.76^\circ$)	35
4.10	Double diamond schematic	36
4.11	Zero field splitting double diamond	37
4.12	Theta correction schematic	38
4.13	Spectroscopic measurements of single diamonds at $\phi = 16^\circ, 79^\circ$	39
4.14	Spectroscopic measurements of double diamond at $\phi = 48.1^\circ$	40
4.15	Double diamond Fano resonance	40
4.16	Eigenvalues of double diamond	41
4.17	Spectroscopic measurements versus ϕ for $ B = 6.2$ mT	42
5.1	GdW ₃₀ level scheme	45
5.2	Nanomagnet transmission spectrum for different temperatures	46
5.3	Nanomagnet before and after experiment	47

Chapter 1

Introduction

In conventional information technology everything starts with the simple question: "0 or 1?", resulting in the basic unit of information, the bit. With the information at hand the question arises, how can it be both retained and processed? Any system capable of binary output, as easy as two sides of a coin, can be used as a bit. One of the most efficient way is processing done via transistors, with which quick manipulation of the bit is possible. After the information is processed, it can be stored inside of magnets for an extended period of time. While the effort to increase processing speeds as well as storage density persists, these systems have a natural limit due to physics. More complex problems still can be solved in finite times with better algorithms, however, some like prime factorization [31], seem to be out of reach for conventional computation.

Utilizing the principles of superposition and entanglement the basic workings of computation changes. Firstly, the simple question of the bit changes to a more complex one: "How 0 or 1?", leading to the basic unit of quantum computation the qubit. Secondly, entanglement of the qubits gives a different set of tools extending the capabilities of information technology. The qubits need a different type of quantum binary system, capable of long time storage and fast processing of the quantum information. Suitable mediums for qubits are atoms, electron spins, nuclear spins and superconducting devices.

The requirements for a quantum computation were formulated by Di Vincenzo in the form of 5 criteria [8] for the system:

- Qubits have to be well defined and their number scalable.
- Capable of initialization to a starting quantum state, e.g. all spins down.
- High isolation from the environment, to guarantee long coherence times.

- Controlled unitary transformation applicable, which form the basis of quantum logic gates.
- Complete qubits state readout possible, with maximal information transfer.

The preservation of the qubit phase is a major challenge as it can be lost by coupling to the environment. Using systems which are better isolated overall come with the downside of slower processing, as the system applying the manipulation is also better isolated. Similar to classical computing for which not every bit system is suitable for every task, not a single qubit system is superior in all aspects. This leads to the idea of hybrid quantum systems (HQS), where different qubit systems are combined via a quantum bus [38].

The main interest of this work lies in the storage and transfer of quantum information. The counterpart of storage of classic information in magnets can be realized with electron and nuclear spins, utilizing their longer coherence times up to seconds [26]. More specific, the quantum information is stored in an ensemble of spins to increase the coupling strength, with the downside of reduced coherence time. This is tolerable, as the main aspect of the measurements in this work is the coherent information transfer between two spin ensembles via a quantum bus.

Experimental Hybrid Quantum System

In the experiment the two components of the hybrid quantum system are the spin ensemble, formed by negatively charged Nitrogen Vacancies (NV^-) in diamond, and the quantum bus, realised by microwave resonators. The NV^- has a transition in the microwave regime from a ground state $|g\rangle$ to an excited state $|e\rangle$, identified as the qubit state $|0\rangle$ and $|1\rangle$ respectively. The transition frequency can be tuned magnetically to the resonator frequency. The microwave resonator acts as a cavity increasing the coupling to the spin ensembles placed on top of it. By applying a probe field to the resonator the transition from $|0\rangle$ to $|1\rangle$ is driven and the qubit flips between those states. The coupling of the resonator field to the spin ensemble is seen in the transmission spectrum of the resonator. An avoided crossing is formed at the point of overlap between the spin transition frequency and the resonance frequency. The transmission is suppressed for a field with the resonance frequency, while for frequencies above and below a new transmission maximum is formed. To test coherent information transfer via a quantum bus, two ensembles are placed on top of the resonator. The form of the avoided crossings in the transmission spectrum, during individual and complete overlap of the transition frequencies with the resonator frequency, is observed. The behaviour of the avoided crossings is used to prove coherent information transfer between the two spin ensembles via the quantum bus.

Chapter 2

Theory

In this chapter a theoretical approach for interaction of a spin ensemble with an electromagnetic field inside a cavity is presented. The transmission spectrum of the cavity is calculated, which is compared to the measurement. In Section 2.1 the model for interaction between a two level system and the field of a single mode is shown. The model is expanded up to an ensemble of two level systems exhibiting collective effects. The necessary parameters which have to be measured for a mathematical description are defined. Afterwards the utilized spin system, nitrogen vacancy centres in diamond, is explained in Section 2.2. In Section 2.3 two types of cavities used in the experiment are introduced, $\lambda/2$ resonators and lumped element resonators. Section 2.4 covers the applied method of transmission calculation via scattering theory.

2.1 Spin-Field Interaction

2.1.1 Tavis Cummings Model

The interaction of a spin ensemble with a single mode electromagnetic field in a cavity is described by the Tavis Cummings model [34, 35]. It originates from the Rabi model [30], which describes a two level system coupled to an external field. The Rabi Hamiltonian has the form [2]

$$\begin{aligned} H_{Rabi} &= H_F + H_S + H_{Int} \\ &= \hbar\omega_c a^\dagger a + \frac{\hbar\omega_s}{2} \sigma^z + \hbar g(a + a^\dagger)(\sigma^+ + \sigma^-) \end{aligned} \tag{2.1}$$

where a^\dagger and a are the creation and annihilation operator of the single mode field and σ^z , $\sigma^\pm = \sigma^x \pm i\sigma^y$ are Pauli matrices of the two level system. ω_c is the cavity mode frequency, ω_s the transition frequency of the two level system and g describes the coupling strength. Considering only magnetic interaction the coupling strength is $g = \mathbf{B}(\mathbf{r}) \cdot \boldsymbol{\mu}/\hbar$. It is dependent on the magnetic field of the photon in the cavity, $\mathbf{B}(\mathbf{r})$, as well as the magnetic moment, $\boldsymbol{\mu}$, of the transition. The magnetic field in the cavity is proportional to $\frac{1}{\sqrt{V_c}}$ [5], where V_c is the cavity mode volume. This will be relevant for cavity size consideration later on.

In Eq. (2.1) $a^\dagger\sigma^+$ and $a\sigma^-$ are the counterrotating terms. They describe creation of a photon and simultaneous excitation of the two level system and vice versa. If the normalized coupling rate $\frac{g}{\omega_c}$ is sufficiently small the counterrotating terms can be neglected in the rotating wave approximation, leading to the Jaynes Cummings model [20]. For the ensembles later introduced, with dimensions of MHz for collective g and GHz for cavity frequency, this condition is satisfied since $\frac{g}{\omega_c} < 1\%$. In the ultrastrong coupling regime, where the dimension of the effective coupling is similar to the cavity frequency, the Jaynes Cummings model breaks down, as seen in Niemczyk et al. [28].

Expanding the Jaynes Cummings model for a single two level system, without the counterrotating terms, to N two level systems (spins) results in the Tavis Cummings model. With the N systems tightly packed inside a solid body the coupling to a single mode field occurs with the same coupling strength g . The corresponding Hamiltonian [18], in an ideal system without losses, has the form

$$H_{TC} = \hbar\omega_c a^\dagger a + \frac{\hbar\omega_s}{2} \sum_{j=1}^N \sigma_j^z + \hbar g \sum_{j=1}^N (a\sigma_j^+ + a^\dagger\sigma_j^-) \quad (2.2)$$

For the study of collective effects of the spins inside the ensemble the Dicke model [6] is used. For the so called Dicke states all spins are considered as a single entity. To obtain these kind of states all individual spin operators have to be combined. Following Henschel et al. [18] and Garraway [15], the collective atomic operators can be defined as

$$\begin{aligned} S^+ &= \sum_{j=1}^N \sigma_j^+ = \sum_{j=1}^N |e_j\rangle \langle g_j| \\ S^- &= \sum_{j=1}^N \sigma_j^- = \sum_{j=1}^N |g_j\rangle \langle e_j| \\ S^z &= \frac{1}{2} \sum_{j=1}^N \sigma_j^z = \frac{1}{2} \sum_{j=1}^N (|e_j\rangle \langle e_j| - |g_j\rangle \langle g_j|) \end{aligned} \quad (2.3)$$

Rewriting the Hamiltonian for individual spin operators into the collective form leads to

$$H_{TC} = \hbar\omega_c a^\dagger a + \hbar\omega_s S^z + \hbar g(aS^+ + a^\dagger S^-) \quad (2.4)$$

The collective angular momentum operations have the form $\mathbf{S} = (S^x, S^y, S^z)^T$ and $S^\pm = (S^x \pm iS^y)$. The eigenstates of \mathbf{S}^2 and S^z can be arranged into the Dicke states $|J, M\rangle$.

According eigenvalues are $\mathbf{S}^2 |J, M\rangle = J(J+1) |J, M\rangle$ and $S^z |J, M\rangle = M |J, M\rangle$, with $J = 0, \dots, N/2$ and $M = -J, \dots, J$. The collective ground state is $|J, -J\rangle = |g, g, \dots, g\rangle$ the fully inverted excited state is $|J, J\rangle = |e, e, \dots, e\rangle$. Other states can be reached with S^\pm as

$$S^\pm |J, M\rangle = \sqrt{(J \pm M + 1)(J \mp M)} |J, M \pm 1\rangle \quad (2.5)$$

The number of possible combination states for N spins is 2^N , with many degenerate states leading to $|J, M\rangle$. The simplest case of two spins leads to 4 Dicke states

Super-Radiant		Sub-Radiant
$ 1, 1\rangle = e_1, e_2\rangle$		$ 0, 0\rangle = \frac{1}{\sqrt{2}} (e_1, g_2\rangle - g_1, e_2\rangle)$
$ 1, 0\rangle = \frac{1}{\sqrt{2}} (e_1, g_2\rangle + g_1, e_2\rangle)$		
$ 1, -1\rangle = g_1, g_2\rangle$		

(2.6)

States with $J = 1$ are called super-radiant, whereas for $J = 0$ sub-radiant. The sub-radiant state does not couple to the cavity since the ladder operators in the coupling term lead to $S^\pm |0, 0\rangle = 0$. This means whereas super-radiant states interact with the photons in the cavity, sub-radiant states do not. For an ensemble with N spins in the collective ground state, excitation by a single photon only produces the fully symmetric super radiant state $|J, -J+1\rangle = \frac{1}{\sqrt{N}} (|e, g, \dots, g\rangle + |g, e, \dots, g\rangle + \dots + |g, g, \dots, e\rangle)$. All other states for which $J < N/2$ are sub-radiant and can not be accessed by the single photon. Coherently overlapping two distinct symmetric states produces a new symmetric state and an antisymmetric state. This property will be used later as a proof that the vanishing of the antisymmetric state in the transmission spectrum, after an overlap of states, indicates coherent coupling of separated ensembles.

For high polarisation of the spins (low temperatures) and excitation in the range of single photons the number of collective spins $N \gg n_{ex}$. This can be utilized to simplify the Hamiltonian by transforming the non commuting collective atomic operators S^\pm and S^z to commuting bosonic operators. This is described by the Holstein Primakoff approximation [19].

Following Kurucz et al. [23] and Garraway [15] the bosonic spin operators b_j and b_j^\dagger are written as

$$\begin{aligned} S^z &= -\frac{N}{2} + b^\dagger b \\ S^+ &= (S^-)^\dagger = b^\dagger \sqrt{N - b^\dagger b} \approx \sqrt{N} b^\dagger \end{aligned} \quad (2.7)$$

With the number of excitation n_{ex} , corresponding to $b^\dagger b$, much lower than the number of spins N follows, $\sqrt{N - b^\dagger b} = \sqrt{N} \sqrt{1 - b^\dagger b/N} \approx \sqrt{N}$. The Hamiltonian can be rewritten, disregarding the constant factor $-\frac{N}{2} \hbar \omega_s$, as

$$H_{TC} = \hbar \omega_c a^\dagger a + \hbar \omega_s b^\dagger b + \hbar g_{eff} (ab^\dagger + a^\dagger b) \quad (2.8)$$

where $g_{eff} = \sqrt{N}g$ for spins with equal coupling strengths. For different coupling strengths this changes to $g_{eff} = \sqrt{\sum_{j=1}^N g_j^2}$.

b^\dagger is the creation operator of the afore mentioned symmetric collective excitation, which is the only mode that couples to the cavity. Applying the operator to the ground state $|0\rangle_s = |J, -J\rangle = |g, g, \dots, g\rangle$ leads to the excited state $|1\rangle_s = b^\dagger |J, -J\rangle = |J, -J + 1\rangle = \frac{1}{\sqrt{N}}(|e, g, \dots, g\rangle + |g, e, \dots, g\rangle + \dots + |g, g, \dots, e\rangle)$, with $b^\dagger = \frac{1}{\sqrt{N}} S^+ = \frac{1}{\sqrt{N}} \sum_{j=1}^N \sigma_j^+$. The coupling strength of this single collective excitation scales with \sqrt{N} whereas all other possible Dicke states become sub-radiant. This enhancement of \sqrt{N} is another property showing coherent coupling between spins.

2.1.2 Solution of Tavis Cummings

In an experimental setup losses are present, which have to be included in the theoretical model. A microwave resonators is used as cavity, which has a photon leakage rate described by the full width at half maximum (FWHM) of $\kappa = 1/\tau$. In the ensemble the spins have a loss rate of γ (FWHM). The experimental setup including losses is depicted in Fig. 2.1.

In the experiment a probing signal with frequency ω is applied to the cavity. For varying ω the transmission through the cavity is measured. Transmission calculations can be done with the input and output formalism [14]. In this formalism an arbitrary system is coupled to a "heat bath" of harmonic oscillators. The Hamiltonian has the form $H = H_{Sys} + H_{Bath} + H_{Int}$. Using the time evolution of an operator A as basis, $\frac{dA}{dt} = -\frac{i}{\hbar}[A, H]$, the Quantum Langevin equation is derived (time dependency of the operators is omitted)

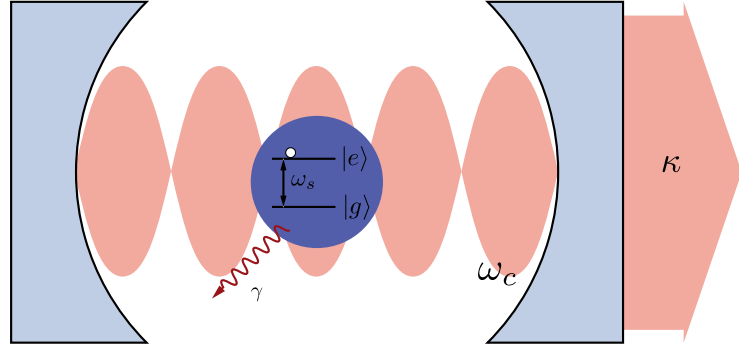


FIGURE 2.1: Representation of experimental setup including photon losses in the cavity, κ , and losses in the spin ensemble, γ . The spin ensemble interacts with a single mode field of frequency ω_c in the microwave cavity. With the spin ensemble transition frequency $\omega_s = \omega_c$ transitions from the ground to the excited state occur.

$$\dot{A} = -\frac{i}{\hbar}[A, H_{sys}] - \left\{ [A, C^\dagger] \left(\frac{\alpha}{2}C + \sqrt{\alpha}B_{in} \right) - \left(\frac{\alpha}{2}C^\dagger + \sqrt{\alpha}B_{in}^\dagger \right) [A, C] \right\} \quad (2.9)$$

where A and C are arbitrary system operators (e.g. a, b of H_{TC}), α is a loss parameter (FWHM) and B_{in} is the input-field. Next to the input-field a transmission-field is defined as $B_t = B_{out} - B_{in} = \sqrt{\alpha}C$.

Following Diniz et al. [7], applying the H_{TC} from Eq. (2.8) as H_{sys} , two equations for the cavity operator a and spin operator b are obtained. In the case of the operator a in Eq. (2.9) the loss parameter is chosen to be κ with the additional condition that $A = C = a$. Additionally a noise term f_a has to be included to conserve commutation relations. The equations are written in the frame rotating with the probe frequency ω for the transmission spectrum. This leads to

$$\begin{aligned} \dot{a} &= -\frac{i}{\hbar}[a, H_{TC}] - \left\{ \left(\frac{\kappa}{2}a + \sqrt{\kappa}B_{in} \right) \right\} + f_a \\ \dot{a} &= -i(\omega_c - \omega)a - ig_{eff}b - \frac{\kappa}{2}a - \sqrt{\kappa}B_{in} + f_a \end{aligned} \quad (2.10)$$

with the commutation relations $[a, a^\dagger] = [b, b^\dagger] = 1$, $[a, a] = [a, b] = [a, b^\dagger] = 0$. Similarly for the spin operator b the loss parameter is defined as γ , $A = C = b$ and a noise term f_b is included. However there is no in-field term for this Langevin equation

$$\begin{aligned} \dot{b} &= -\frac{i}{\hbar}[b, H_{TC}] - \left\{ \left(\frac{\gamma}{2}b \right) \right\} + f_b \\ \dot{b} &= -i(\omega_s - \omega)b - ig_{eff}a - \frac{\gamma}{2}b + f_b \end{aligned} \quad (2.11)$$

The complex transmission is calculated with the average of B_t and B_{in} (noise terms vanish) with $t(\omega) = \frac{\langle B_t \rangle}{\langle B_{in} \rangle}$. Solving Eqs. (2.10) and (2.11) for steady states ($\dot{a} = \dot{b} = 0$) gives the input-field as

$$B_{in} = \frac{a}{\sqrt{\kappa}} \left[-i(\tilde{\omega}_c - \omega) + i \frac{g_{eff}^2}{(\tilde{\omega}_s - \omega)} \right] \quad (2.12)$$

where $\tilde{\omega}_c = \omega_c - i\frac{\kappa}{2}$ and $\tilde{\omega}_s = \omega_s - i\frac{\gamma}{2}$ incorporate the losses in complex frequencies. With $B_t = \sqrt{\kappa}a$ this leads to the transmission coefficient

$$t(\omega) = \frac{\kappa}{-i \left[(\tilde{\omega}_c - \omega) - \frac{g_{eff}^2}{(\tilde{\omega}_s - \omega)} \right]} = \frac{i\kappa(\tilde{\omega}_s - \omega)}{\left[(\tilde{\omega}_c - \omega)(\tilde{\omega}_s - \omega) - g_{eff}^2 \right]} \quad (2.13)$$

The points of interest in the transmission spectrum are the positions for which the square of the absolute value of the transmission $|t(\omega)|^2$ has a maximum. The corresponding probe frequency ω can be calculated by setting the denominator of the transmission to 0, following [3]. Solving the quadratic equation for ω and multiplying the result with \hbar gives the eigenenergies $E^\pm = \hbar\omega^\pm$ of the Tavis Cummings model

$$\begin{aligned} E^\pm &= \hbar \frac{\omega_s + \omega_c}{2} - i\hbar \frac{\kappa + \gamma}{4} \pm \hbar \sqrt{g_{eff}^2 + \frac{[(\omega_c - i\frac{\kappa}{2}) - (\omega_s - i\frac{\gamma}{2})]^2}{4}} \\ E^\pm &= \hbar \frac{\omega_s + \omega_c}{2} - i\hbar \frac{\kappa + \gamma}{4} \pm \frac{\hbar}{2} \sqrt{4g_{eff}^2 - \left[\frac{\gamma - \kappa}{2} - i\Delta \right]^2} \end{aligned} \quad (2.14)$$

with the detuning $\Delta = (\omega_c - \omega_s)$. The real part of E^\pm corresponds to the peak positions and the imaginary part to the peak (half) widths. Depending on the detuning two regimes can be defined, the resonant regime for which $\Delta = 0$ and the dispersive regime for which $\Delta \gg (g_{eff}, \frac{\kappa}{2}, \frac{\gamma}{2})$. The resonant regime can be further divided into strong coupling and weak coupling.

For strong coupling the coupling strength g surpasses the losses γ and κ . This leads to two distinct real parts of E^\pm , since the term under the root is positive. An avoided crossing is formed as the degeneracy of the peak position, corresponding to the eigenvalues E^+ and E^- , is lifted. The distance between the two peaks is proportional to the coupling strength. In the experiment the effective coupling strength of the spin system can therefore be identified by measuring the peak distance of the maximal transmission values on resonance.

In the case of weak coupling losses outweigh the coupling strength, which leads to the root contribution only in the imaginary part of the eigenvalues. The peak positions are degenerate with the coupling strength only influencing the peak widths, generating an overlap of two peaks with different widths. In the weak regime determination of coupling strength is highly impractical.

2.1.3 Resonant Regime

With detuning $\Delta = 0$ the corresponding eigenstates for the eigenvalues E^\pm are [18]

$$\begin{aligned} |+\rangle &= \frac{1}{\sqrt{2}}(|1\rangle_s |0\rangle_c + |0\rangle_s |1\rangle_c) \\ |-\rangle &= \frac{1}{\sqrt{2}}(|1\rangle_s |0\rangle_c - |0\rangle_s |1\rangle_c) \end{aligned} \quad (2.15)$$

where $|0\rangle_c$ is the cavity ground state and $|1\rangle_c = a^\dagger |0\rangle_c$ is the state for a single photon in the cavity. The spin ensemble states are $|0\rangle_s = |J, -J\rangle = |g, g, \dots, g\rangle$, for the ground state, and $|1\rangle_s = b^\dagger |0\rangle_s = |J, -J+1\rangle = \frac{1}{\sqrt{N}}(|e, g, g, \dots, g\rangle + |g, e, g, \dots, g\rangle + \dots + |g, g, g, \dots, e\rangle)$, for the symmetric super-radiant state for a single excitation. Other ensemble states with essentially one excitation are sub-radiant.

Strong Coupling

On resonance the term under the root is positive with the condition $2g_{eff} > |\frac{\gamma-\kappa}{2}|$, which leads to

$$\begin{aligned} Re\left(\frac{E^\pm}{\hbar}\right) &= \omega_c \pm \frac{1}{2}\sqrt{4g_{eff}^2 - \left(\frac{\gamma-\kappa}{2}\right)^2} \\ Im\left(\frac{E^\pm}{\hbar}\right) &= -\frac{\kappa+\gamma}{4} \end{aligned} \quad (2.16)$$

On resonance the transmission shows two peaks, each with a FWHM of Γ with $\frac{\Gamma}{2} = \frac{\kappa+\gamma}{4}$. However to distinguish between those two peaks the additional condition for strong coupling $g_{eff} \gg \frac{\kappa}{2}, \frac{\gamma}{2}$ has to be fulfilled. In the strong coupling regime these two peaks are split by the vacuum Rabi splitting $\Omega = \omega^+ - \omega^- = \sqrt{4g_{eff}^2 - \left(\frac{\gamma-\kappa}{2}\right)^2} \approx 2g_{eff}$. An avoided level crossing occurs which can be seen in Fig. 2.2a. The plot shows the resonant regime as well as the dispersive regime, discussed in the next section.

Weak Coupling

With $2g_{eff} < |\frac{\gamma-\kappa}{2}|$ the eigenvalues are

$$\begin{aligned} Re\left(\frac{E^\pm}{\hbar}\right) &= \omega_c \\ Im\left(\frac{E^\pm}{\hbar}\right) &= -\frac{\kappa+\gamma}{4} \pm \frac{1}{2}\sqrt{\left(\frac{\gamma-\kappa}{2}\right)^2 - 4g_{eff}^2} \end{aligned} \quad (2.17)$$

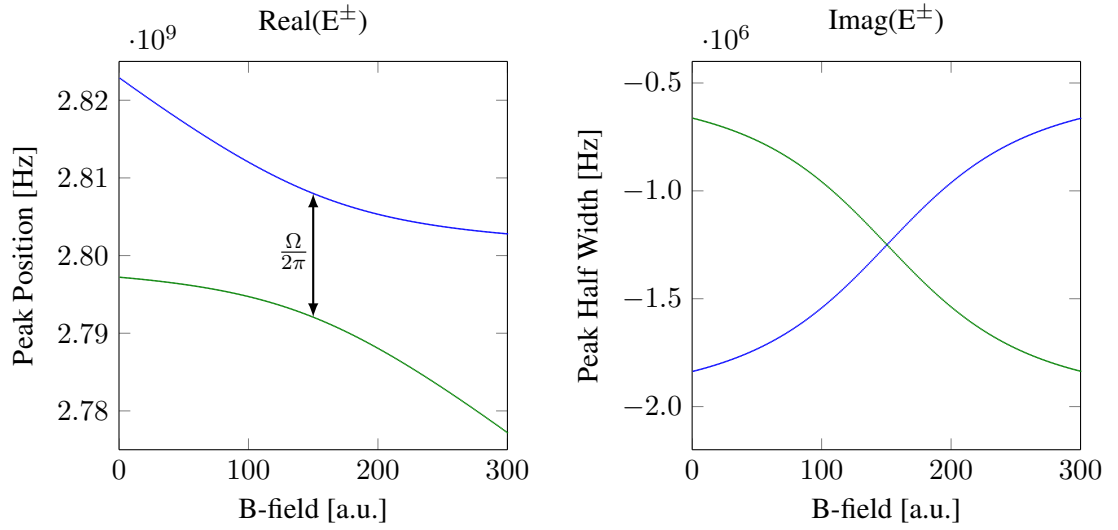


FIGURE 2.2: Tavis Cummings eigenvalues E^\pm for strong coupling. The spin system is assumed to be linearly tuned (from 2.82 GHz to 2.78 GHz) by an arbitrary magnetic field, crossing the constant resonator frequency (at 2.8 GHz). The parameters are set to $(g_{eff}, \frac{\kappa}{2}, \frac{\gamma}{2}) = 2\pi \cdot (8, 0.5, 2)$ MHz. The real parts of E^\pm , corresponding to the peak positions, show two distinct values with the spin transition frequency on resonance with the cavity frequency. In comparison the imaginary parts are degenerate for $\omega_c - \omega_s = \Delta = 0$.

Since the real part has only a single value there is no avoided crossing of the transmission. The single peak is a superposition of two peaks with different FWHM, which are dependent on the coupling strength, as seen in Fig. 2.3b.

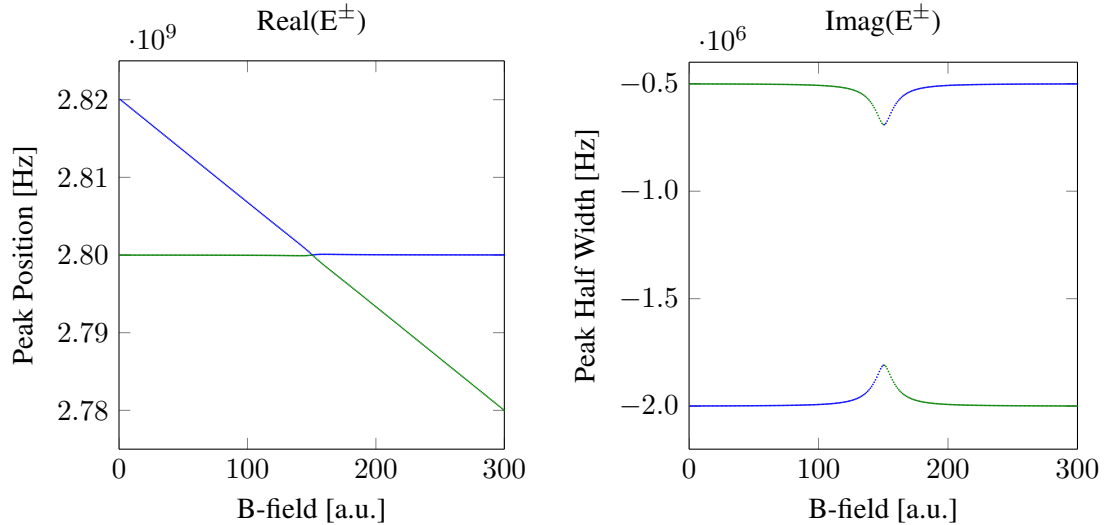


FIGURE 2.3: Tavis Cummings eigenvalues E^\pm for weak coupling. Only the coupling strength is reduced to $g_{eff} = 2\pi \cdot 0.5$ MHz in comparison to the prior figures. For $\Delta = 0$ there is no avoided crossing in the peak positions and the peak widths are not degenerate. This leads to two peaks with different widths superimposed instead of an avoided crossing.

2.1.4 Dispersive Regime

In the dispersive regime the detuning $\Delta = (\omega_c - \omega_s) \gg (g_{eff}, \frac{\kappa}{2}, \frac{\gamma}{2})$. Rewriting the square root term of Eq. (2.14) gives

$$\begin{aligned} \Delta \sqrt{1 + \frac{2i(\frac{\gamma-\kappa}{2})}{\Delta} + \frac{4g_{eff}^2 - (\frac{\gamma-\kappa}{2})^2}{\Delta^2}} &= \Delta \sqrt{1+x} = \Delta(1 + \frac{x}{2} - \frac{x^2}{8} + O[x^3]) = \\ &= \Delta + \frac{\Delta}{2} \left(\frac{2i(\frac{\gamma-\kappa}{2})}{\Delta} + \frac{4g_{eff}^2 - (\frac{\gamma-\kappa}{2})^2}{\Delta^2} \right) - \frac{\Delta}{8} \left(\frac{-4(\frac{\gamma-\kappa}{2})^2}{\Delta^2} + O\left[\frac{1}{\Delta^3}\right] \right) = \\ &= \Delta + i\left(\frac{\gamma-\kappa}{2}\right) + \frac{2g_{eff}^2}{\Delta} + O\left[\frac{1}{\Delta^2}\right] \end{aligned} \quad (2.18)$$

This expansion gives the two eigenvalues

$$\begin{aligned} \frac{E^+}{\hbar} &\approx \frac{\omega_s + \omega_c}{2} + \frac{\Delta}{2} + \frac{g_{eff}^2}{\Delta} - i\frac{\kappa}{2} = \omega_c + \frac{g_{eff}^2}{\Delta} - i\frac{\kappa}{2} \\ \frac{E^-}{\hbar} &\approx \frac{\omega_s + \omega_c}{2} - \frac{\Delta}{2} - \frac{g_{eff}^2}{\Delta} - i\frac{\gamma}{2} = \omega_s - \frac{g_{eff}^2}{\Delta} - i\frac{\gamma}{2} \end{aligned} \quad (2.19)$$

With the spin system far detuned from the cavity the peak widths become uncoupled, as indicated in Fig. 2.2b, since the imaginary parts do not include g_{eff} . The positions are uncoupled except for the correction term $\Delta_{disp} = \frac{g_{eff}^2}{\Delta}$ called the dispersive shift.

2.2 Spin System NV^-

The main spin ensemble considered in this work consists of negatively charged defects in diamond, so called NV^- [9, 10, 36, 38]. These defects are formed by a substitutional Nitrogen (N), replacing a carbon atom, adjacent to a carbon Vacancy (V), as seen in Fig. 2.4. The nitrogen atom is covalently bound to 3 carbon atoms leaving 2 electrons unbound. The 3 carbon atoms surrounding the vacancy each have 1 unbound electron. Therefore, with an additional electron from the crystal the NV^- centre is composed of 6 electrons. The spin density of the unpaired electrons is highly localized in the vacancy. The spin density at the nitrogen on the other hand is only 2%.

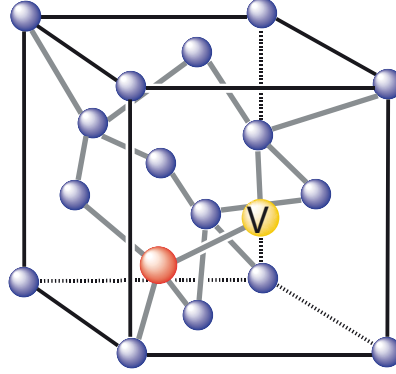


FIGURE 2.4: NV crystal structure with a substitution nitrogen atom in red next to a vacancy.

2.2.1 Electronic Ground State

The NV centre has a paramagnetic ground state (3A_2) of spin $S = 1$, producing a triplet with the m_s states $|0\rangle$, $|\pm 1\rangle$. The transition frequencies between $|0\rangle \rightarrow |\pm 1\rangle$ are in the microwave regime and can be Zeeman tuned. Furthermore, optical transitions from the electronic ground state to an electronic excited state (3E) exist. In this work only the microwave transitions are utilized. However, there is a need for optical transitions in regard to initializing and readout of states.

The basic Hamiltonian of a spin $S = 1$ system has the form $H = H_{zfs} + H_Z = h\mathbf{S}^T \bar{D} \mathbf{S} + g_e \mu_b \mathbf{B} \mathbf{S}$ [21, 37], with a zero field term (ZFS) and a Zeeman term. In the zero field term \bar{D} is the zero field splitting tensor. The Zeeman splitting term includes the electronic g-factor $g_e \approx 2$, μ_b the Bohr magneton and \mathbf{B} the magnetic field. Converting the Bohr magneton $\frac{\mu_b}{h} = \beta \approx 14 \frac{\text{MHz}}{\text{mT}}$ gives a tuning factor of $g\beta \approx 28 \frac{\text{MHz}}{\text{mT}}$. The pure m_s states $|\pm 1\rangle$ are therefore tuned by $28 \frac{\text{MHz}}{\text{mT}}$ relative to the unchanged $|0\rangle$ for a magnetic field in the z direction.

Other terms can be included for the interaction with nuclear spins, especially for the isotopes ${}^{13}\text{C}$, ${}^{14}\text{N}$. However, ${}^{13}\text{C}$ has a low natural abundance of 1.1 % and does not strongly couple as an ensemble. The interaction with neighbouring ${}^{14}\text{N}$ (natural abundance 99.6 %) is small due to the small probability density of the unpaired electrons at the nitrogen site. For the conducted measurements these terms usually have minor influence and are not included in the calculations. Exceptional is the situation for which the ${}^{13}\text{C}$ sub ensemble is on resonance with the resonator for zero field, as in Section 4.1.

The zero field splitting tensor \bar{D} describes anisotropic spin-spin interaction of the two electrons making up the ground state. This tensor lifts the degeneracy of the states $m_s = -1, 0, 1$ at zero field. \bar{D} is diagonal in its eigenframe and traceless, therefore, it can be described with two

parameters D and E . The D parameter is responsible for the splitting of $|0\rangle$ and $|\pm 1\rangle$, while E produces an additional split between $|-1\rangle$ and $|+1\rangle$. Following Stoll and Schweiger [33] the zero field splitting Hamiltonian can be written in the form $H_{zfs}/h = \bar{D}_x S_x^2 + \bar{D}_y S_y^2 + \bar{D}_z S_z^2 = D(S_z^2 - S(S+1)/3 \cdot \mathbb{1}) + E(S_x^2 - S_y^2)$. For $S = 1$ adding an energy of $\frac{2}{3}D \cdot \mathbb{1}$ to the Hamiltonian shifts the ground state to zero energy.

The complete spin Hamiltonian for NV⁻ in the S_z basis is given as

$$\begin{aligned} \frac{H_{spin}}{h} &= \begin{matrix} & | +1 \rangle & | 0 \rangle & | -1 \rangle \\ \begin{matrix} \langle +1 | \\ \langle 0 | \\ \langle -1 | \end{matrix} & \begin{pmatrix} D + g_e \beta B_z & g_e \beta \frac{B_x - i B_y}{\sqrt{2}} & E \\ g_e \beta \frac{B_x + i B_y}{\sqrt{2}} & 0 & g_e \beta \frac{B_x - i B_y}{\sqrt{2}} \\ E & g_e \beta \frac{B_x + i B_y}{\sqrt{2}} & D - g_e \beta B_z \end{pmatrix} \end{matrix} = \\ &= D S_z^2 + E(S_x^2 - S_y^2) + g_e \beta \mathbf{BS}. \end{aligned} \quad (2.20)$$

The transition frequencies f_- from $|0\rangle \rightarrow |-1\rangle$ as well as f_+ from $|0\rangle \rightarrow |+1\rangle$ are calculated by taking the difference of the corresponding eigenvalues. This leads to $\omega_- = 2\pi f_- = 2\pi(\frac{E_- - E_0}{h})$ and $\omega_+ = 2\pi f_+ = 2\pi(\frac{E_+ - E_0}{h})$. These transition frequencies can be Zeeman tuned into resonance with the cavity, in order to produce an avoided crossing. Due to the E parameter level mixing occurs, which means that for low magnetic fields m_s is not a good quantum number. With high enough magnetic fields the Zeeman term is dominating the spin Hamiltonian, which reduces the mixing ratio. Since the E parameter is small for NV diamonds a magnetic field of 1 mT is enough to counteract the level mixing and m_s is considered to be a good quantum number for the whole system.

In Fig. 2.5 the eigenvalues of the NV Matrix are plotted with a magnetic field applied in the z direction. The parameters used are $D = 2.8$ GHz and $E = 0.3$ GHz, which is more than a factor 10 smaller in the experiment for better illustration. Therefore, the significant level mixing of the m_s states due to the higher E term is ignored and the pure states $|0\rangle$ and $|\pm 1\rangle$ are used as label. Thermal excitation depolarizes the ensemble reducing the number of collective spins capable of induced transitions by the photon in the cavity and therefore decreases the effective coupling strength. The working temperature of 70 mK in the experiment produces a polarisation degree above 75 % for the NV⁻ ensemble with transitions at about 2.8 GHz.

Without an external magnetic field the eigenvalues are $\frac{E_0}{h} = 0$, $\frac{E_+}{h} = (D + E)$ and $\frac{E_-}{h} = (D - E)$. The zero field parameters are measured by applying a pump tone to the NV spin system, in addition to the probe field, without an external magnetic field [4]. At zero field the

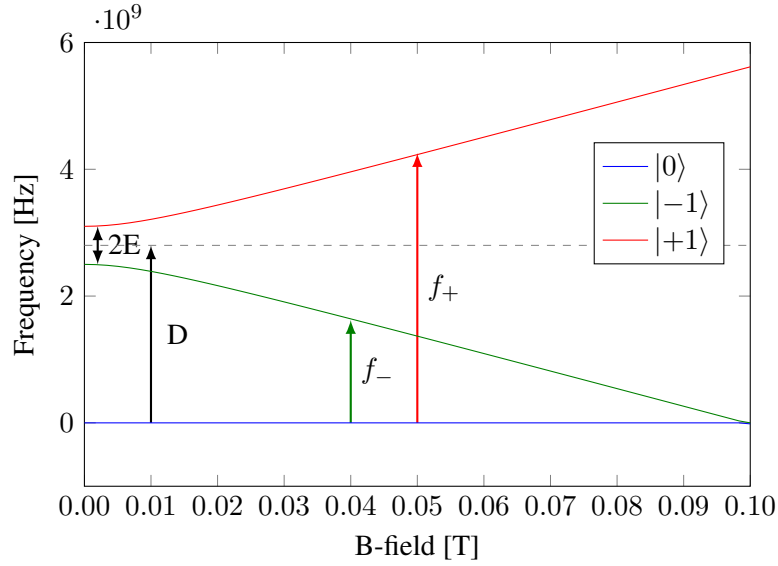


FIGURE 2.5: NV eigenvalues tuned by a magnetic field in z direction with the zero field parameters D and E . The E parameter is assumed to be larger than it is in the experiment to enhance visibility. The transition frequency utilized in the experiment is f_- from $|0\rangle \rightarrow |-1\rangle$ at approximately 2.8 GHz

cavity frequency and the spin transition frequencies are detuned from each other and the cavity frequency corresponds to $\omega_c + \frac{g_{eff}^2}{\Delta}$ with the dispersive shift $\Delta_{disp} = \frac{g_{eff}^2}{\Delta}$. The spins are depolarized by the probe tone, reducing the effective coupling g_{eff}^2 , and the dispersive shift is removed. The biggest depolarization of the spins occurs for the pump frequency at the exact location of the spin transitions, which are given by D and E . The scanning of the pump frequency produces two peaks in a maximal shift plot, with a peak distance of $2E$ and a mean peak position of D .

The NV for this work are produced with diamonds of the type Ib, with higher nitrogen concentrations, which are irradiated with either neutrons or electrons to produce vacancies. Irradiation damages create a distinct E parameter, whereas for pure NV^- systems E is assumed to be approximately 0 [21].

2.2.2 Defect Reference Frame

The NV^- s are implemented inside a crystal structure, therefore, their quantisation axis can not be chosen freely, it is dependent on the crystal orientation. NV^- is a point defect with a C_{3v} symmetry [27] with four $\langle 111 \rangle$ crystallographic directions (chosen as $[1\ 1\ 1]$, $[-1\ -1\ 1]$, $[-1, 1, -1]$, $[1, -1, -1]$). This leads to four subclasses of NV^- centres, which experience external magnetic fields in the laboratory frame differently.

The magnet field applied in the lab frame $(B_x, B_y, B_z) = ([1\ 0\ 0], [0\ 1\ 0], [0\ 0\ 1])$ has to be converted into the defect frame (V_x, V_y, V_z) , in the following case for the direction $[1\ 1\ 1]$

$$\begin{pmatrix} V_x \\ V_y \\ V_z \end{pmatrix} = \begin{pmatrix} \frac{1}{\sqrt{6}} & \frac{1}{\sqrt{6}} & \frac{-2}{\sqrt{6}} \\ \frac{1}{\sqrt{2}} & -\frac{1}{\sqrt{2}} & 0 \\ \frac{1}{\sqrt{3}} & \frac{1}{\sqrt{3}} & \frac{1}{\sqrt{3}} \end{pmatrix} \begin{pmatrix} B_x \\ B_y \\ B_z \end{pmatrix} \quad (2.21)$$

where the matrix consists of the unit vectors of the NV^- centres. For the other crystallographic directions the matrix only differs in sign in the corresponding column.

As seen in Fig. 2.6 for a magnetic field in the (001) plane at least two subclasses are tuned equally (same colour in the lattice). In the case of a magnetic field in the direction x $([1\ 0\ 0])$ or y $([0\ 1\ 0])$ all four sub ensembles experience the same field amplitude. The plots in Fig. 2.7 show the transition frequencies f_{\pm} for each pair of subensembles, corresponding to the colours in the projection, for either varying magnetic field amplitude with a fixed angle ϕ or vice versa. The parameters used are $D = 2.88\text{ GHz}$ and $E = 10\text{ MHz}$ matching the values found for NV diamonds in the experiment. Every field out of the (001) plane produces unwanted splitting of the sub ensembles, therefore, a smooth contact area is advantageous for optimal experiment control. Offsets can be adjusted with an applied field in the z $([0\ 0\ 1])$ direction, however, depending on the cavity used the applicable z field amplitude is limited.

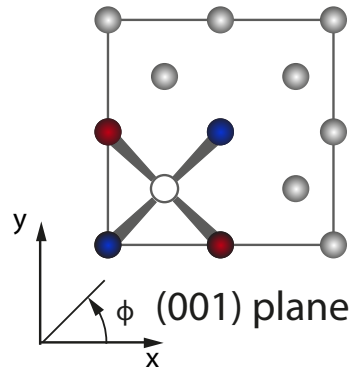


FIGURE 2.6: Projection of 4 NV directions to the (001) plane. In this projection, fields applied in plane tune at least a pair of NV directions, with the same colour, by the same amount. With the field plane angle $\phi = 0^\circ$ (x direction) or $\phi = 90^\circ$ (y direction) all 4 NV directions are tuned equally by an applied magnetic field.

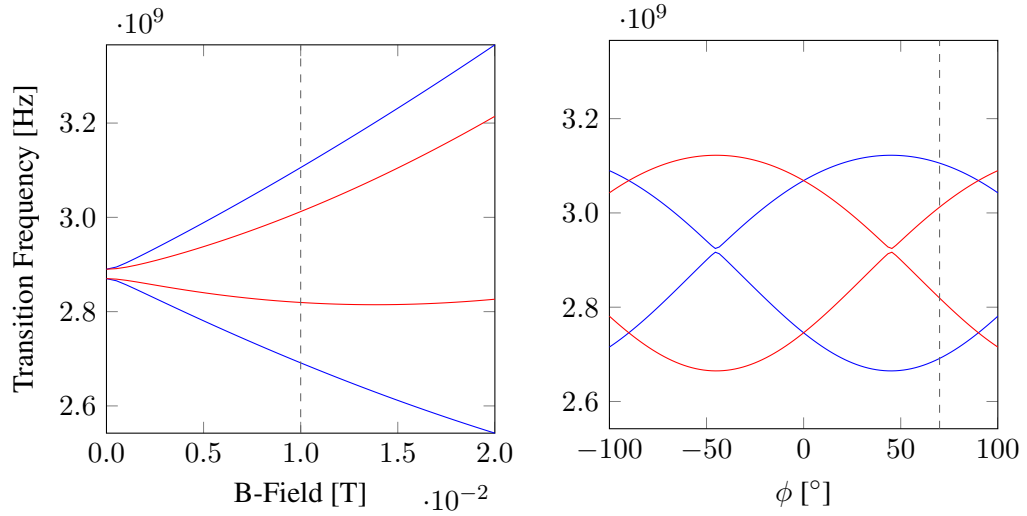


FIGURE 2.7: Transition frequencies f_{\pm} for each pair of subensembles for either constant magnetic field angle $\phi = 70^\circ$ or amplitude $B = 10$ mT. Lines of the same colour belong to the same sub ensemble pair with each a f_+ and f_- transition. Each line consists of two transitions for two equally tuned subensemble directions. The dashed line corresponds to the fixed value used in the other plot.

2.3 Cavity

In the experiment cavities are implemented by means of microwave resonators. This type of cavity can be reliably designed for frequencies in the GHz regime. Two types of resonators are utilized with certain advantages and disadvantages, $\lambda/2$ resonators and Lumped Element Resonators (LER).

2.3.1 Basic Principle of Microwave Resonators

Lumped Element Resonant Circuit

Near resonance the basic properties of a microwave resonator can be shown by means of a lumped element parallel LCR circuit, following Pozar [29]. The basic schematic of a parallel LCR circuit is shown in Fig. 2.8 with an input impedance of

$$Z_{in} = \left(\frac{1}{R} + \frac{1}{i\omega L} + i\omega C \right)^{-1} \quad (2.22)$$

The resonance frequency is given by $\omega_0 = \frac{1}{\sqrt{LC}}$ at which the imaginary part of the impedance is zero and $|Z_{in}|^2 = R^2$, as seen in Fig. 2.9. The FWHM can be expressed like before as κ and is the distance between the points for which $|Z_{in}|^2$ has half of it's maximum value, $\frac{R^2}{2}$.

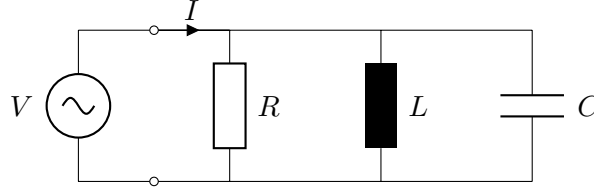


FIGURE 2.8: Lumped parallel LCR circuit schematic used to illustrate microwave resonator properties near resonance.

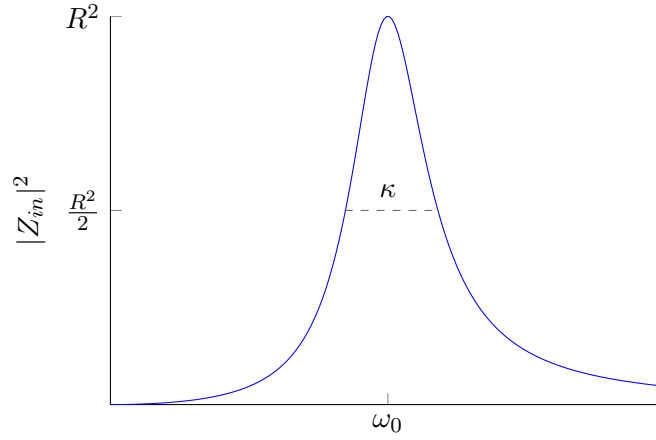


FIGURE 2.9: Input impedance Z_{in} dependent on the frequency used. With an applied frequency corresponding to the resonance frequency ω_0 the impedance becomes real, with $Z_{in} = R$. A feedline with an impedance $Z = R$ couples the maximal power into the resonator for an applied field with the resonance frequency. The FWHM κ for a microwave resonator corresponds to photon loss.

An important quantity with regards to loss in the cavity is the quality factor Q . The Q factor is defined as

$$Q = \omega_0 \frac{W_e + W_m}{P_{loss}} \quad (2.23)$$

where W_e is the stored electric energy in the capacitor C , W_m is the magnetic energy stored in the inductor L and P_{loss} is the power dissipated in the resistor R . It gives the ratio of average energy stored to energy lost per oscillation cycle. In the case of parallel LCR circuit $Q = \omega_0 RC$.

By defining $\omega = \omega_0 + \Delta\omega$ and assuming $\Delta\omega$ to be small Eq. (2.22) can be rewritten as

$$Z_{in} \approx \frac{R}{1 + 2iQ\Delta\omega/\omega_0} \quad (2.24)$$

In Fig. 2.9, with the normalized frequency $\frac{\omega}{\omega_0} = \frac{\omega_0 + \Delta\omega}{\omega_0} = 1 + \frac{\Delta\omega}{\omega_0}$, the FWHM points occur at $\frac{\Delta\omega}{\omega_0} = \pm \frac{1}{2} \frac{\kappa}{\omega_0}$, which is applied to Eq. (2.24). At this point $|Z_{in}|^2 = \frac{R^2}{2} = \frac{R^2}{1 + 4Q^2(\kappa/2\omega_0)^2}$ which leads to the relation $\kappa = \frac{\omega_0}{Q}$.

The prior defined Q factor is an internal parameter of the resonator used. Coupling to other circuits reduces the quality factor and gives a total Q factor of

$$\frac{1}{Q_{tot}} = \frac{1}{Q_{int}} + \frac{1}{Q_{ext}} \quad (2.25)$$

with Q_{int} from the resonator and Q_{ext} from external circuits. The coupling coefficient is defined as $g = \frac{Q_{int}}{Q_{ext}}$. At $g = 1$ the external circuit and the resonator are critically coupled and the power transfer is at a maximum. The resonator is undercoupled for $g < 1$ and overcoupled for $g > 1$.

Overcoupled resonators and therefore low Q are used for fast measurements of the spin state of the ensembles. Undercoupled resonators with high Q are utilized for long time storage of photons in the cavity [17].

Transmission Line Resonator (TLR)

For the TLR the LCR components are reproduced by distributed elements of a terminated transmission line, instead of lumped elements. The termination of a transmission line with a load impedance different from its characteristic impedance creates reflections. These reflections superimpose with incoming waves producing varying voltages and currents over its length. Therefore the input impedance can be controlled with different termination and position of the load.

The type of TLR relevant for this work is the open-circuited $\lambda/2$ line, which behaves like a parallel resonant circuit for a signal wavelength of $\lambda/2$ or multiples of $\lambda/2$. It has the input impedance of

$$Z_{in} = \frac{Z_0}{\alpha l + i\Delta\omega\pi/\omega_0} \quad (2.26)$$

where Z_0 is the characteristic impedance of the TL, α is the attenuation constant and l the length of the TL. The unloaded Q for this resonator is $Q_0 = \frac{\pi}{2\alpha l}$.

Coplanar Wave Guide (CPW)

Resonators are coupled to the measurement setup via a superconducting CPW transmission line. CPW are planar transmission lines used in the microwave regime with low radiation losses [32]. They are fabricated on a dielectric substrate and consist of a centre strip conductor and ground planes on both sides, see Fig. 2.10. Its characteristic impedance (usually 50Ω) is determined by the ratio $\frac{w}{w+2g}$, where w is the width of the centre conductor and g its distance from the ground planes. Therefore, keeping the same ratio the CPW can be made as small as necessary while keeping the same impedance. There is a limitation due to fabrication once the roughness of the used material becomes relevant for small dimensions of the CPW.

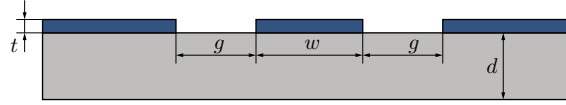


FIGURE 2.10: Coplanar wave guide structure. Keeping the same ratio $\frac{w}{w+2g}$ the impedance can be kept constant while decreasing the size of the transmission line.

The CPW and all resonators in the experiment are etched into superconducting niobium metal on a sapphire substrate.

2.3.2 $\lambda/2$ Resonator

For $\lambda/2$ resonators the centre conductor of the CPW is interrupted at two locations. This produces a transmission line resonator with open ends which capacitively couples to the CPW feed line. The length of the TLR specifies the resonance frequency and the coupling capacitors with capacitances of C_{in} and C_{out} dictate the loaded quality factor Q .

Due to their small width they exhibit large field strengths. This is a result of the before mentioned field strength proportionality to $\frac{1}{\sqrt{V_c}}$, with V_c as the cavity volume. However the length of the $\lambda/2$ resonator is restricted by the used wavelength.

Applying a field with a wavelength of $\lambda/2$ to the resonator leads to a single magnetic field maximum in the cavity, the position at which an ensemble is placed. In contrast for a wavelength of λ two field maxima are present in the cavity. In the experiment two ensembles are placed on the resonator which has to act as a full wave resonator for the desired resonance frequency. Therefore, a full wave resonator has to be twice as long as a half wave resonator for the same resonance frequency.

2.3.3 Lumped Element Resonator (LER)

For LER the resonance is produced by lumped elements, capacitor and inductor, etched into the niobium metal.

In the case of LER the cavity dimension is considerably smaller than that of a $\lambda/2$ resonator. Therefore the amount of spins necessary to reach strong coupling is lower, assuming similar losses, since the interaction with each individual spin is stronger. Theoretically this can be utilized to investigate spin ensembles with small contact area, either due to roughness and or size. Furthermore the small size of the LER makes it more robust against out of plane fields, hysteresis effects appear at larger magnetic field amplitudes. Since magnetically coupling is utilized placing the ensemble on the inductor is preferential.

Disadvantageously is that placement of the ensemble is more crucial since the LER can easily be missed.

2.4 Implementation of Tavis Cummings

As discussed before the transmission coefficient and the eigenenergies can be calculated for a single ensemble system with Eqs. (2.13) and (2.14). In the case of NV⁻ at least 4 individual sub ensembles have to be considered due to their symmetry. Each ensemble has two transition frequencies ω_- and ω_+ corresponding to $|0\rangle \rightarrow |\pm 1\rangle$, which all can differ depending on the magnetic field. Furthermore, combining diamond samples, different losses and couplings for the ensembles have to be included.

Therefore an equivalent method is utilized which easily can be expanded to calculate transmission and eigenenergies. The method is based on scattering theory applying Green's function [11]. The system is described via a Hamiltonian of the form

$$\frac{H_{sys}}{\hbar} = \begin{matrix} & |1 \downarrow\downarrow\rangle & |0 \uparrow\downarrow\rangle & |0 \downarrow\uparrow\rangle \\ \begin{matrix} \langle 1 \downarrow\downarrow| \\ \langle 0 \uparrow\downarrow| \\ \langle 0 \downarrow\uparrow| \end{matrix} & \begin{pmatrix} \omega_c - i\frac{\kappa}{2} & g_1 & g_2 \\ g_1 & \omega_{s_1} - i\frac{\gamma_1}{2} & 0 \\ g_2 & 0 & \omega_{s_2} - i\frac{\gamma_2}{2} \end{pmatrix} \end{matrix} \quad (2.27)$$

In this matrix ω_c is the cavity mode frequency with according FWHM loss κ . Two ensembles are included with the transition energies $\omega_{s_1}/\omega_{s_2}$, the coupling strengths g_1/g_2 and FWHM losses γ_1/γ_2 . The eigenvalues of this matrix are the coupled eigenenergies of the cavity and the ensembles.

To calculate the transmission in the cavity a probe frequency ω is applied. The matrix T is calculated with

$$T(\omega) = \left((H_{sys}/\hbar - \omega \cdot \mathbb{1}) \right)^{-1} \quad (2.28)$$

The transmission coefficient is given by $t(\omega) = C \cdot T(1, 1)$, with the element T(1,1) corresponding to the cavity matrix element in H_{sys} . The constant factor C, for the correct normalization of the transmission amplitude, can be found comparing $T(1, 1)$ with Eq. (2.13).

Assuming the simple case that ensemble 1 and 2 are identical leads to the T matrix of the form

$$T = \begin{pmatrix} \tilde{\omega}_c - \omega & g & g \\ g & \tilde{\omega}_s - \omega & 0 \\ g & 0 & \tilde{\omega}_s - \omega \end{pmatrix}^{-1} \quad (2.29)$$

$$T(1, 1) = \frac{(\tilde{\omega}_s - \omega)}{(\tilde{\omega}_c - \omega)(\tilde{\omega}_s - \omega) - 2g^2}$$

Comparing the solution with Eq. (2.13) shows that for the correct amplitude $i\kappa$ has to be multiplied with $T(1,1)$, therefore, $t(\omega) = i\kappa \cdot T(1, 1)$. The multiplication factor depends only on the cavity used and is not influenced by type or amount of spin systems. Furthermore, $g_{eff}^2 = 2g^2$ agrees with the established increase of effective coupling with \sqrt{N} , since the same ensemble is used twice and therefore $g_{eff} = \sqrt{2}g$.

In the experiment the transmission includes an additional constant, the average photon number in the cavity n_{avg} , which leads to $|t(\omega)|^2 = n_{avg}^2 \cdot |i\kappa \cdot T(1, 1)|^2$. The average photon number can be determined by measuring $|t(\omega)|^2$ at the centre of the avoided crossing for $\Delta = (\omega_c - \omega_s) = 0$, where the transmission only depends on $(g_{eff}, \frac{\kappa}{2}, \frac{\gamma}{2})$ and n_{avg} . The parameters $(g_{eff}, \frac{\kappa}{2}, \frac{\gamma}{2})$ can be determined by other means which leaves n_{avg} directly correlated to the measured $|t(\omega)|^2$. With the two ensembles in Eq. (2.27) the average photon number becomes

$$n_{avg} = |t(\omega = \omega_c = \omega_{s1/s2})| \cdot \left(\frac{\frac{\kappa}{2} \frac{\gamma_1 \gamma_2}{2} + \gamma_1 g_2^2 + \gamma_2 g_1^2}{-\kappa \frac{\gamma_1 \gamma_2}{2}} \right) \quad (2.30)$$

2.4.1 Measurement Requirements

To summarize, the following experimental conditions have to be fulfilled to utilize the theoretical approach. The coupling strength of the spin system should suffice $g_{eff} \gg \frac{\kappa}{2}, \frac{\gamma}{2}$ to guarantee strong coupling, however, $\frac{g_{eff}}{\omega_c}$ needs to be small enough for the rotating wave approximation to be valid. Spins inside the ensemble should be tightly packed so that they experience a similar coupling g . For the Holstein Primakoff approximation high spin numbers and low photon numbers are needed for the condition $N \gg n_{ex}$. Therefore, low temperatures are crucial due to an exponential decay of spin polarisation.

To compare the theoretical model with the measurements the parameters in the system Hamiltonian of Eq. (2.27) have to be determined. The spin transition frequencies ω_s , corresponding to the applied magnetic field, are calculated with the difference of eigenvalues of the spin Hamiltonian

of Eq. (2.20). The necessary parameters D and E are measured in the dispersive regime, with an applied pump tone in addition to the probe tone. The parameters $(g_{eff}, \frac{\kappa}{2}, \frac{\gamma}{2})$ and the cavity frequency ω_c have to be determined via the transmission spectrum.

The resonator parameters $\frac{\kappa}{2}$ and ω_c can be measured by removing the influence of the spins in the ensemble. The dielectric loading due to the ensemble material, which is independent of the spins, is still included in $\frac{\kappa}{2}$. Detuning the frequency of the spin and the ensemble (dispersive regime) and probing in the vicinity of the cavity frequency leads to a transmission peak with a FWHM $\approx \kappa$. Alternatively by increasing the temperature the spins lose their polarisation and their influence on the cavity. With a temperature at about 500 mK all materials used are still superconducting, therefore no increase in losses, and the spins mostly depolarized. Increasing the temperature has the advantage that all spins are reliably depolarized and is therefore used for the following measurements. In comparison in Fig. 2.2b the influence of the spin system is still present at a detuning of 20 MHz.

On resonance approximately $2g_{eff}$ corresponds to the distance of the two transmission peaks. In some cases for weaker strong coupling the full form of the vacuum Rabi splitting should be applied. The FWHM of both peaks at the avoided crossing is $\Gamma = \frac{\kappa + \gamma}{2}$ which leads to γ with the prior measured κ .

Chapter 3

Measurement Setup

In this chapter the measurement setup is described, which can be seen in Fig. 3.1. Starting with the main container of the experiment, the adiabatic demagnetization refrigerator (ADR) in Section 3.1. The concept of the ADR is discussed as well as the components summarized. In the second part the used measurement devices, the Vector Network Analyzer (VNA) (Section 3.2) and the Microwave Generator (MG) (Section 3.3) are outlined. Lastly an overview of the used resonators is given with their individual specifications in Section 3.4.

3.1 Adiabatic Demagnetization Refrigerator (ADR)

The containment vessel of the experiment is a pulse tube ADR Cryostat of the model 103 Rainier produced by the company High Precision Devices (HPD). It has four stages with approximate temperatures 55 K, 4.2 K, 1 K and < 55 mK operating in high vacuum. The two upper stages are cooled by a pulse tube refrigerator using helium. Adiabatic demagnetisation of two different paramagnetic salt pills is utilized to cool the two lower stages. The salts are placed inside a bore of the ADR magnet. The colder stages are mounted on a metal rod which are in contact with the corresponding paramagnetic salt. Of interest in this experiment is the stage at 50 mK, which uses Ferric Ammonium Alum (FAA) pills.

At the beginning of the cooldown the lower stages are brought into thermal contact with the upper stages via a heat switch. The whole system is cooled down with the pulse tube to a temperature of about 3 K. Once this temperature is reached the ADR magnet field is gradually increased polarizing the paramagnetic salts. This reduces the magnetic entropy and consequently the temperatures of the salts rise due to total entropy conservation. Further cooling removes this additional heat. Afterwards the heat switch is opened uncoupling the lower stages from the higher ones. The magnet is adiabatically turned down, which reduces the temperature as

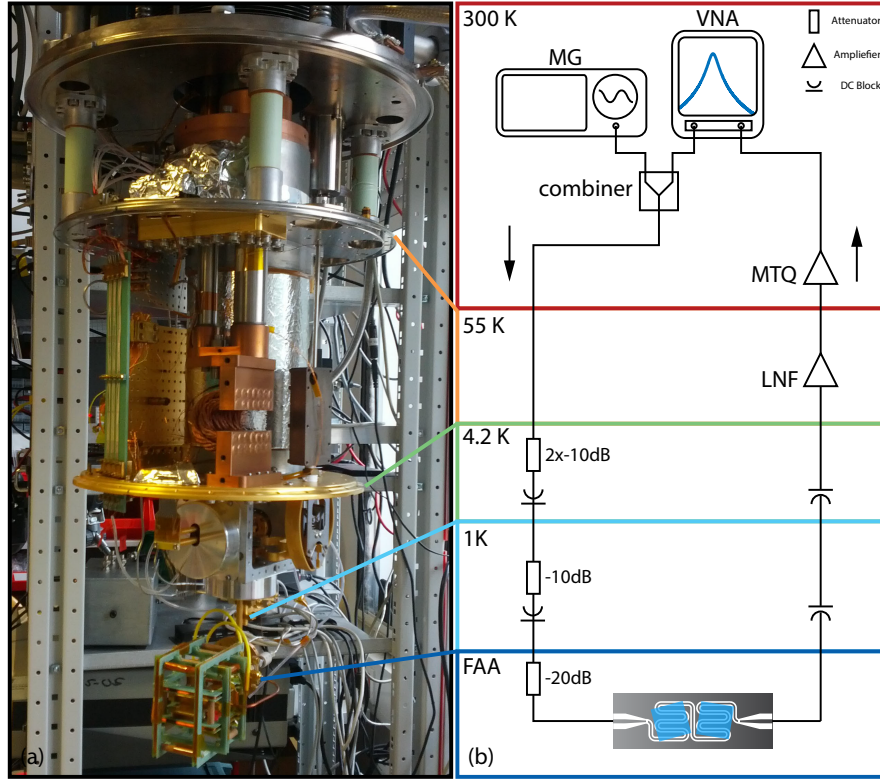


FIGURE 3.1: Measurement setup. On the left picture is the unshielded ADR with the coil setup and the experiment on the bottom stage. At this stage temperatures below 55 mK can be reached. The probe tone is applied to the resonator by the VNA, which can be combined with an additional microwave pump signal from the MG. Including all 4 attenuators and the cables in and outside the ADR the total attenuation of the signal down to the experiment is -60 dB. The signal going back to the VNA is amplified by a low noise cryogenic amplifier (LNF) as well as a room temperature amplifier (MITEQ) each with a gain of about 40 dB.

the magnetic entropy increases. The lower temperatures of the salts extract heat from the cold stages cooling them further down to 50 mK. The stage can be kept on this temperature as long as there is remaining magnetic field, which translates to a cooling energy. After the cooling energy is consumed the whole process has to be repeated.

The measured resonator is placed on the lowest stage with an operation temperature of 70 mK. This temperature can be kept stable for about 10 hours, if there is no significant additional heat introduced by microwaves. Attenuators are used to prevent thermal noise reaching the lower stages. The attenuation inside the ADR down to the resonator is about -57 dB, including cable losses as well as attenuators. This gives a total attenuation of about -60 dB, including the cables leading to the ADR. The applied power settings in the measurement section have this attenuation already added. Exiting the resonator the signal is amplified by low noise amplifiers towards the VNA.

In addition to the ADR magnet responsible for cooling, three Helmholtz coils are installed on the 50 mK stage to apply magnetic fields to the spin system. The coils are arranged in the

form of a cage each producing a magnetic field in one of the three space coordinates. They are able to provide a magnetic field up to 15 mT. The ADR magnet is shielded and should only produce a magnetic field offset of 0.2 mT at most. In Fig. 3.2 the resonator can be seen inside the Helmholtz coil cage.

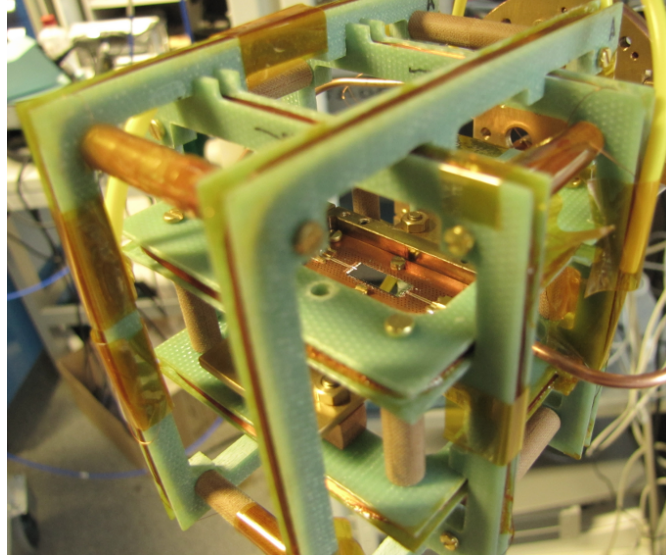


FIGURE 3.2: 3D Helmholtz coils setup with the containment box of the resonator. Cooper coaxial cables, seen on the right, apply the signal from the VNA to the sample box.

3.2 Vector Network Analyzer (VNA)

In all the experiments transmission measurements through the resonators are utilized. For this purpose a VNA is used, which can provide changes of amplitude and phase in a frequency range of 4 kHz to 9 GHz. The VNA is initialized by shorting the cables leading into the ADR to normalize the signal. Afterwards probe signals are applied in the microwave regime in the vicinity of the resonator frequency. With the signal ratio of $\frac{\text{Transmitted}}{\text{Incident}}$ the complex transmission parameter $S_{21} = t$ is given as output. The transmission parameter is plotted in the form of $10 \cdot \log_{10}|t|^2$ giving the attenuation of the signal in decibel. Typical VNA parameters used are an output power of -10 dBm, IF bandwidth of 100 Hz and frequency range of 100 MHz with 401 equidistant measurement points.

The resonance peak is fitted in the complex domain with a Lorentzian function of the form

$$t = A \cdot e^{-i\phi} e^{-i\omega dt} \frac{-i\frac{\Gamma}{2}}{\omega - \omega_0 - i\frac{\Gamma}{2}} \quad (3.1)$$

with the probe frequency ω , resonance frequency ω_0 , FWHM Γ , global phase angle ϕ , phase shift parameter dt and amplitude A .

The function contains 5 fit parameters which have to be identified. With the dimensions of the resonance frequency in GHz, FWHM in MHz and transmission amplitude < 1 rescaling has to be applied for the fitting. For this the probe frequency range of the VNA is scaled to an area of 0.5 to 1.5, with $\omega_{sc} = 0.5 + \frac{\omega - \min(\omega)}{\max(\omega) - \min(\omega)}$. The complex transmission is normalized to 1 by dividing it by the factor t_{max} , which is the absolute maximum of both the real and imaginary part of the transmission. The scaled fit parameters are

$$\begin{aligned}
 \omega_{0_{sc}} &= 0.5 + \frac{\omega_0 - \min(\omega)}{\max(\omega) - \min(\omega)} \\
 A_{sc} &= A/t_{max} \\
 \Gamma_{sc} &= \frac{\Gamma}{\max(\omega) - \min(\omega)} \\
 dt_{sc} &= dt \cdot (\max(\omega) - \min(\omega)) \\
 \phi_{sc} &= \phi - \omega_0 \cdot dt + \omega_{0_{sc}} \cdot dt_{sc}
 \end{aligned} \tag{3.2}$$

All fits are done numerical with the MATLAB intern function `fminsearch` to find the minimum of $\chi = \sum(|t_{meas} - t_{fit}|^2)$. The fit is quite unstable and the starting parameters have to be chosen carefully. Therefore ω_c , Γ and A should be quite close to the actual value as they can be easily estimated.

The Lorentzian function does not describe the transmission spectrum accurately with deviations depending on the system setup. For an unloaded resonator, without a spin ensemble, there is an additional asymmetry due to Fano resonances. Fano resonances occur due to interference of the resonator signal with the background signal. For a loaded resonator the transmission is changed by both the Fano resonances and the spin influence as in Eq. (2.13). The asymmetry can be included by adding a constant complex Fano term to the complex transmission t . The constant term could be identified fitting Eq. (3.1) with an additional complex parameter. The function with the Fano term can be applied to an empty resonator or an empty like resonator, with an ensemble far off resonance. However, adding 2 additional parameters to the fit makes the fitting even more unstable. The Fano is therefore not included in the basic Lorentzian fit since the important parameters ω_0 and Γ can be determined reasonably well.

Another way to extract the Fano term is a fit utilizing Eq. (2.13). For this fit the transmission is completely determined except for the Fano term. Already identified are the parameters ω_c , $(g_{eff}, \frac{\kappa}{2}, \frac{\gamma}{2})$, n_{avg} and the ZFS parameters. This has to be done with the logarithmic form of the transmission, so that the Fano is sufficiently distinct for the fit to work. The results of this fit can be seen in Chapter 4.

3.3 Microwave Generator (MG)

Using a separate microwave generator an additional microwave signal can be applied which is combined with the VNA signal. With the VNA frequency range set in the vicinity of the resonance frequency the MG signal is applied to the spin ensemble. This is used to depolarize the spins in the ensemble, effectively removing the coupling to the cavity. Since the MG signal frequency is off resonance higher input power has to be applied to counteract the attenuation through the resonator.

3.4 Resonators

There are two types of resonators which are used in the experiments of Chapter 4.

Nr. 270 (Double Diamond)

Full Wave

$$f_{res} = 2.913 \text{ GHz}$$

$$C_{in} = 0.72 \text{ fF}$$

$$C_{out} = 5.70 \text{ fF}$$

Nr. 510 (Berkeley)

Transmission Lumped Element (TLER)

$$f_{res} = 2.834 \text{ GHz}$$

$$C_{in} = C_{out}$$

The resonators are placed in the gap of a printed circuit board (PCB) inside a copper box. On the PCB are CPW connected to the input and output of the sample box. The feedlines of the resonator chip are bonded to the CPW with aluminium wires. Additional bonds are used to ground the chip as well as to hold it in place. The signal transmission to and from the box is done via miniSMP. Figure 3.3 depicts a diamond sample mounted on a TLER inside the sample box.

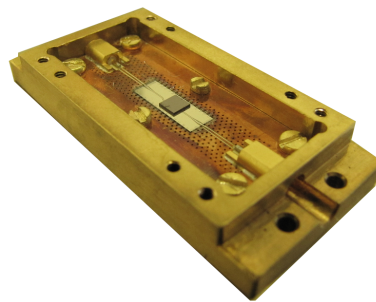


FIGURE 3.3: Resonator box with the bonded resonator chip and a diamond sample placed on top of the resonator. The polished side of the diamond is facing down. Closing the sample box protects the resonator from dirt and produces a cavity preventing fields with unwanted frequencies.

Chapter 4

Measurements and Results

The first part of this chapter, Section 4.1, deals with determination of basic parameters of the NV^- ensembles. This is shown with a single NV^- ensemble provided by a group in Berkeley. The measured parameters are then implemented in the theoretical model and compared to the basic transmission spectrum for varying magnetic fields.

The second part, Section 4.2, shows the feasibility of coherent coupling of two spatially separated NV^- via a resonator. The proof for the coherent coupling is given in two ways. Firstly the coupling strength should increase by $\sqrt{N} \approx \sqrt{2}$ compared to a single ensemble when both ensembles are on resonance with the cavity. Secondly two new Dicke states are produced by superimposing the two radiant Dicke states of each ensemble. One of these states should be radiant, which is the new fully symmetric superposition of both ensembles, and the other should be sub radiant.

For the measurements the VNA applies varying probe tones to the resonator and a transmission spectrum is obtained. The transmission can be influenced with an external magnetic field, which tunes the spin ensemble transition in and out of resonance with the resonator. The magnetic field can be changed in two ways, varying the amplitude at a constant angle and varying the angle with a constant amplitude. Both ways are applied for the following measurements. All plots are depicted in frequency f , therefore, the measured parameters $(g_{eff}, \frac{\kappa}{2}, \frac{\gamma}{2})$ have to be multiplied by 2π since per definition they are corresponding to angular frequency ω .

4.1 Basic Parameters and Optimization

For this series of measurements the NV^- ensemble from Berkeley is measured on resonator Nr.510 (see Section 3.4), which is a TLR with an unloaded resonance frequency of 2.834 GHz.

The initial measurement is the temperature dependency of the resonance frequency and the resonator loss κ . The ADR is cooled down to its lowest temperature and then warms up over time. During the cool down and the warm up the resonance peak is recorded. Relaxation effects up to minutes occur during the cool down producing inaccurate values. The peaks are fitted using Eq. (3.1) to obtain the resonance frequency f_{res} and the quality factor Q , which are plotted in Fig. 4.1.

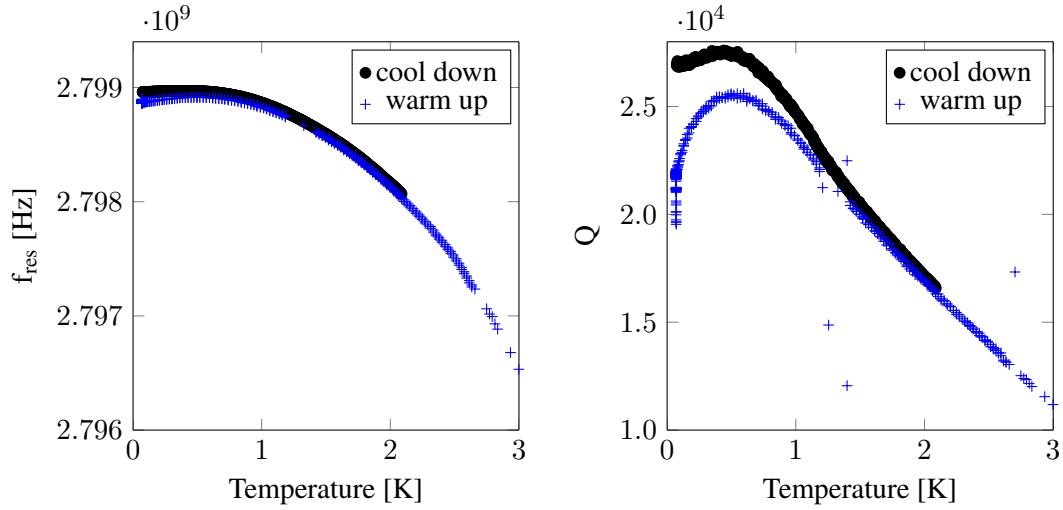


FIGURE 4.1: Temperature dependency of resonance frequency and quality factor during cool down and following warm up. The resonance frequency and the quality factor are obtained by fitting the VNA probe field spectrum. The variation of the measurements originate from long relaxation processes during cool down which can take up to 3 hours. At approximately 500 mK f_{res} and Q have a maximum, at which the spin system is sufficiently depolarized and the components still superconducting. This temperature should be chosen, during warm up, to determine the basic properties f_{res} and Q for an uncoupled resonator. At 1.2 K the aluminium bonds have their transition temperature, which could explain the oscillation seen for Q at that point.

The maximum of the warm up data points at about 500 mK is taken as standard resonance frequency and quality factor. The values are $f_{res} = 2.7989$ GHz and $Q = 25\,500$ which gives a loss of $\frac{\kappa}{2\pi} = \frac{f_{res}}{Q} \approx 0.1$ MHz.

The next step is identification of the zero field parameters D and E via a dispersive measurement. For this the microwave generator is set off resonance to a frequency range in the vicinity of the expected D parameter. With an input pump power of approximately -60 dBm applied to the resonator the MG scans the frequency range depolarizing the spins. This shifts the cavity towards its uncoupled resonance frequency. The biggest shift is produced for a MG frequency corresponding to the NV transition frequency. The VNA probes the resonator near the initial resonance frequency with a power of approximately -90 dBm. The result of the cavity shift depending on the pump frequency is plotted in Fig. 4.2

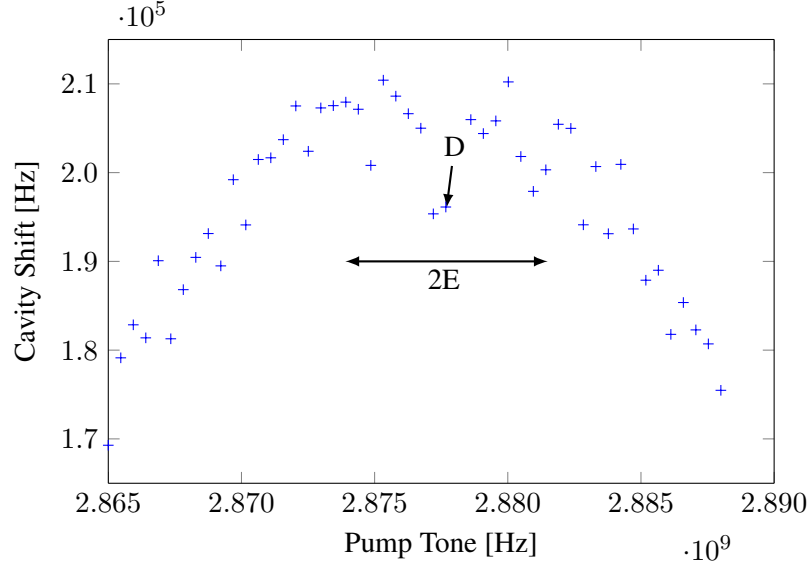


FIGURE 4.2: Dispersive measurement with a pump tone applied in the vicinity of the transition frequencies of the spin system. The polarized spin system is depolarized which results in a reduction of the collective coupling strength and corresponding dispersive shift. The two maxima in the plot are at the frequency of the transitions $|0\rangle \rightarrow (|+1\rangle \pm |-1\rangle)$. Marked are the zero field parameters D and E determining the transition frequencies for zero field.

The resulting zero field parameters are $D = 2.878$ GHz and $E = 3.8$ MHz. Unfortunately one ^{13}C subensemble is on resonance for zero field, due to the close proximity of the cavity resonance frequency to the NV ensemble transition frequency. Therefore, during the measurement an additional shift of the cavity was observed with the initial VNA probe power of -60 dBm. This was prevented by keeping the probe power near -90 dBm for all further measurements with this sample. The lower signal to noise ratio decreased the fitting accuracy, especially for the FWHM, and reduced the visibility of unique features. This measurement series can be used to show basic steps of parameter identification, however, comparison to the theory has to be considered with caution.

The final two parameters which have to be determined are the effective coupling g_{eff} and the ensemble loss $\frac{\gamma}{2}$. These are measured at the avoided crossing. To maximize the coupling and therefore the splitting all 4 sub ensembles have to be tuned equally. With the diamond parallel to the PCB this gives the option of a magnetic field in the x direction with the angles $(\phi = 0^\circ, \theta = 90^\circ)$ or y direction with $(\phi = 90^\circ, \theta = 90^\circ)$. The magnetic field amplitude at which the avoided crossing occurs can be found via a spectroscopic measurement. For this the magnetic field amplitude is increased gradually with the VNA probing in the vicinity of the resonance frequency. The position for which the distance between the split peaks is minimal corresponds to the avoided crossing. Figure 4.3a shows the surface plot for the angles $(\phi = 0^\circ, \theta = 90^\circ)$. The colours represent 10 times the decadic logarithmic attenuation of the normalized transmission of the VNA.

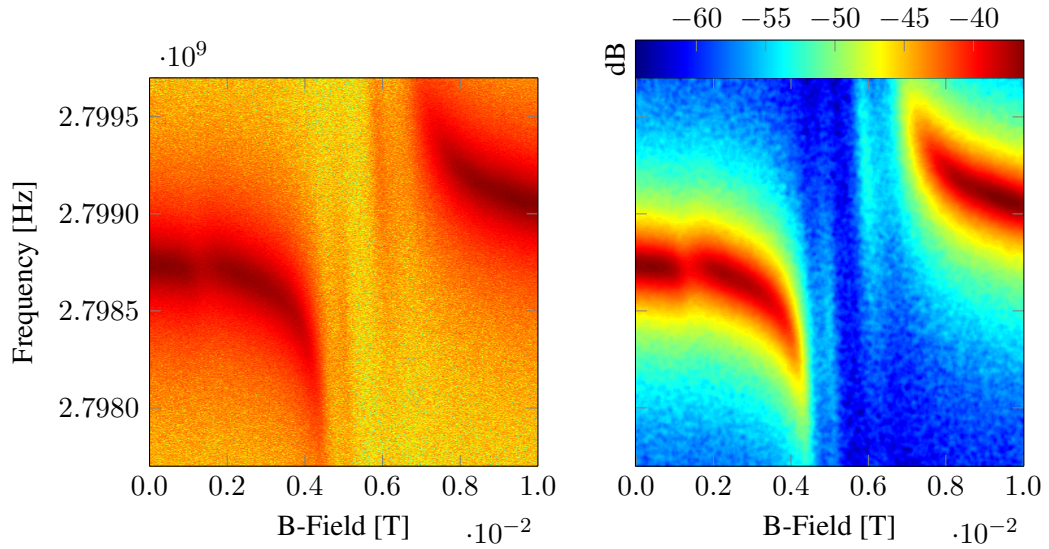


FIGURE 4.3: Spectroscopic transmission measurement for $(\phi = 0^\circ, \theta = 90^\circ)$. The cavity is probed by the VNA with the colours in the plot representing the transmission attenuation in dB. Left is the original measurement, right is the smoothed post processed image. The magnetic field is not yet applied purely in plane producing a splitting of the subensembles resulting in 4 avoided crossings. By aligning the out of plane angle θ at least 2 NV subensembles overlap. With the in plane angle ϕ aligned all 4 subensembles overlap for $\phi = 0^\circ, 90^\circ$.

Due to the low signal to noise, the measurements were post processed in MATLAB by the function SMOOTHN based on the papers of Garcia [12, 13], as seen in Fig. 4.3b. Deviations from a single avoided crossing are due to misaligned fields which split up the subensembles and have to be corrected.

For $\theta \neq 90^\circ$ out of plane fields occur. To measure the angle offset the magnetic field is kept at a constant amplitude at the estimated avoided crossing. The angle ϕ is set to 0° and θ is varied in the vicinity of 90° . The VNA is operated with the same settings as before. The result can be seen in Fig. 4.4.

At the corrected angle $\theta = 90.76^\circ$ the amplitude shows a minimum, when all subensembles overlap with the resonator at the avoided crossing. With all fields kept in plane the plane angle ϕ and magnetic field amplitude for which the maximal splitting occurs have to be identified. For this purpose the VNA is set to a single probe frequency at the resonance frequency. The magnetic field is set to the constant corrected angle $\theta = 90.76^\circ$ with varying amplitude and ϕ . The results of this measurement are shown in Fig. 4.5.

The minimal transmission provides the parameters for the position of the avoided crossing. For a magnetic field amplitude of 5.33 mT and angles $(\phi = 2.46^\circ, \theta = 90.76^\circ)$ all 4 subensembles overlap with their transition frequency matching the resonance frequency. The spectroscopic measurement with the corrected angles can be seen in Fig. 4.6.

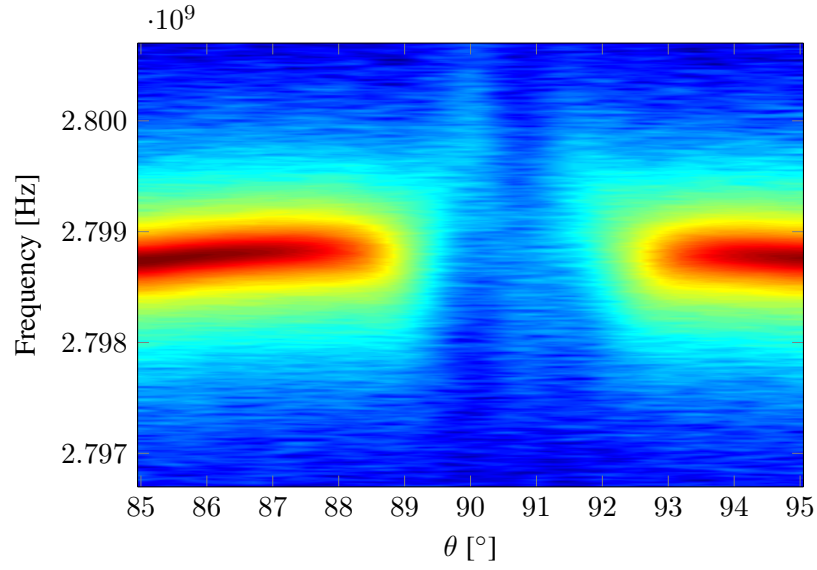


FIGURE 4.4: θ offset measurement with constant $B = 5.4$ mT and $\phi = 0^\circ$. With $\phi = 0^\circ$ all 4 subensembles overlap which produces a single avoided crossing. At $\theta = 90.76^\circ$ the transition shows the sharpest crossing which corresponds approximately to pure in plane fields.

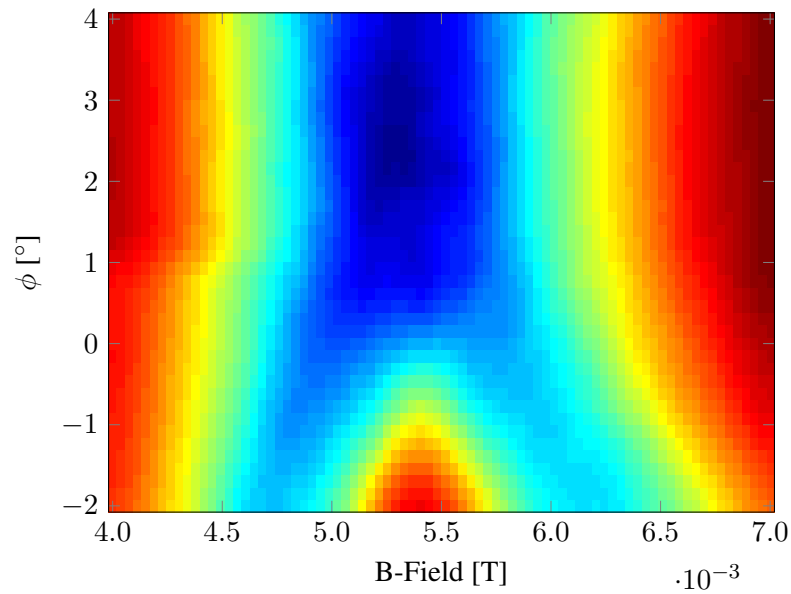


FIGURE 4.5: Measurement for ϕ offset and avoided crossing field amplitude. Fixed are the probe frequency to 2.7989 GHz and $\theta = 90.76^\circ$. With the corrected out of plane angle θ pure in plane fields are applied. Variation of the field amplitude and in plane angle ϕ shows the sharpest avoided crossing at the overlap of all 4 subensembles, appearing at $\phi = 2.46^\circ$ and field amplitude of 5.33 mT.

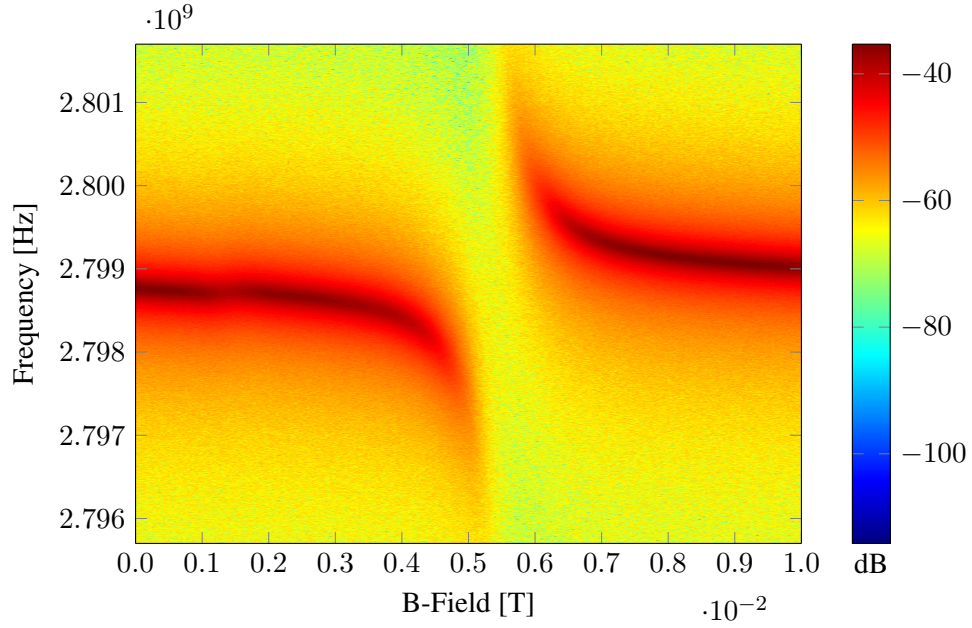


FIGURE 4.6: Spectroscopic transmission measurement with the corrected angles ($\phi = 2.46^\circ, \theta = 90.76^\circ$). The spectroscopy shows a single sharp avoided crossing indicating the correct plane field being applied. The feature at approximately 1.5 mT is produced by weak coupling of one of the ^{13}C subensemble. These are not present in any plots produced by the theoretical approach.

The avoided crossing is clearly evident, however, the two distinct peaks are barely visible. This leads to the conclusion that the parameters are located in the area between weak and strong coupling. Averaging the transmission spectrum at the avoided crossing over 2000 times with an IF Bandwidth of 500 Hz gives Fig. 4.7.

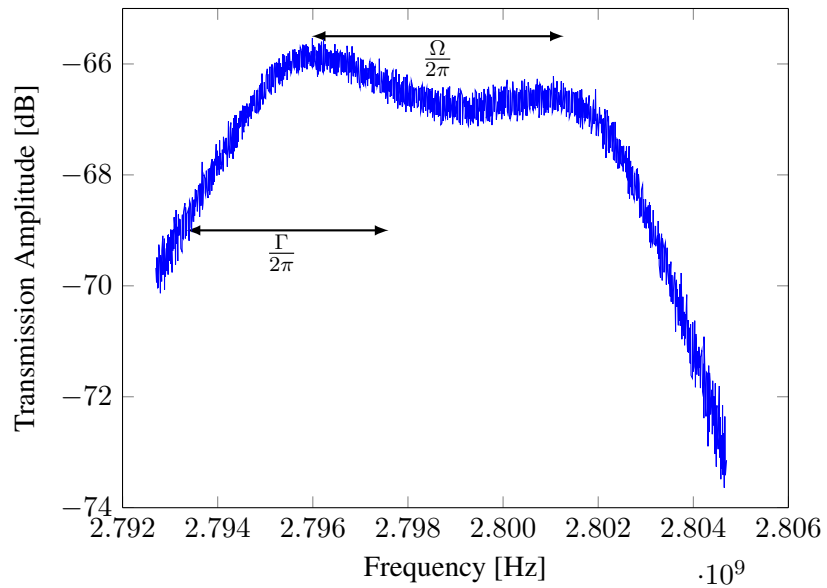


FIGURE 4.7: Transmission amplitude at avoided crossing. Γ is an estimation for the FWHM at -3 dB of the peak maximum. Due to insufficient coupling no clear distinction between the avoided crossing peaks can be made.

The plot shows hints of two peaks with a distance of Ω , the FWHM Γ at -3 dB of the maximum can only be estimated. With the measured values γ is calculated with $\gamma = 2\Gamma - \kappa$, κ can be neglected as it is only 0.1 MHz. Since the parameters are not in the range of strong coupling the full form of the vacuum Rabi splitting is applied $\Omega = \sqrt{4g_{eff}^2 - (\frac{\gamma-\kappa}{2})^2}$ to calculate g_{eff} . The measurement gives $\frac{\Omega}{2\pi} = 5.5$ MHz for 4 subensembles which leads to $\frac{g_{eff}}{2\pi} \approx 3.4$ MHz. To obtain g_{eff} of a single subensemble the factor $\frac{1}{\sqrt{4}}$ has to be multiplied. The estimated value of $\frac{\Gamma}{2\pi} \approx 4.3$ MHz leads to $\frac{\gamma}{2\pi} \approx 8.6$ MHz. The average photon number can be calculated following Eq. (2.30). Converting the measured -67 dB at the centre of the avoided crossing gives $|t(\omega = \omega_c = \omega_{s_{1-4}})| = 10^{-67/10}$ and therefore $n_{avg} = 0.0108$.

The parameters $\omega_c = 2\pi \cdot 2.7989$ GHz and $(g_{eff}, \frac{\kappa}{2}, \frac{\gamma}{2}) = 2\pi \cdot (\frac{3.4}{\sqrt{4}}, 0.1, 4.3)$ MHz are integrated into the T-Matrix, Eq. (2.29), of dimension 9×9 . Its diagonal contains 8 subensemble entries each with their respective transition frequency $\omega_{s_{+1-4}}$ and $\omega_{s_{-1-4}}$, calculated in Eq. (2.20) with the measured parameters $D = 2.878$ GHz and $E = 4$ MHz. All subensembles have the same loss $\frac{\gamma}{2}$ and g_{eff} . The single resonator entry is comprised of f_{res} and $\frac{\kappa}{2}$. The transmission can be calculated with $|t(\omega)|^2 = n_{avg}^2 \cdot |i\kappa \cdot T(1, 1)|^2$. It is plotted as $10 \cdot \log_{10}(|t(\omega)|^2)$ in Fig. 4.8a together with the measurement. The plot shows that the position of the peak maxima and their width agrees well with the measurement, however, there is a tilt present. This tilt is due to Fano resonances which can be included in the calculation by adding a complex constant to the complex transmission $|t(\omega)|^2 = n_{avg}^2 \cdot |i\kappa \cdot T(1, 1) + A_f e^{i\phi_f}|^2$. The value for the Fano amplitude A_f and angle ϕ_f are identified by fitting the logarithmic form of $|t(\omega)|^2$. The obtained values are $A_f = 0.0053$ and $\phi_f = 255^\circ \cdot \frac{\pi}{180^\circ}$ in radian. The corrected calculated transmission is plotted in Fig. 4.8b.

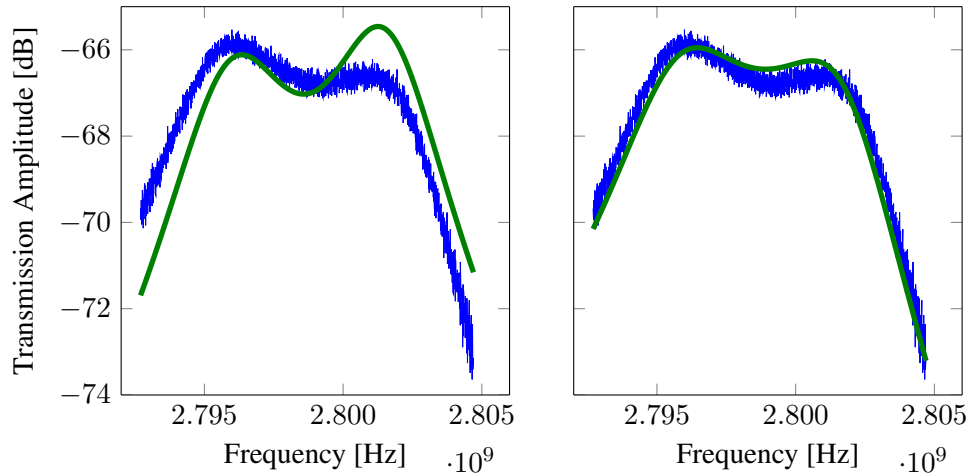


FIGURE 4.8: The green curve in the left plot shows the calculated transmission for the prior measured parameters. In the right plot a constant complex factor is added to the calculated complex transmission corresponding to a Fano resonance.

With all parameters included in the theory the full spectroscopic measurement versus the magnetic field can be calculated for $(\phi = 2.46^\circ, \theta = 90.76^\circ)$. The calculated surface plot can be seen in Fig. 4.9b next to the measurement in Fig. 4.9a.

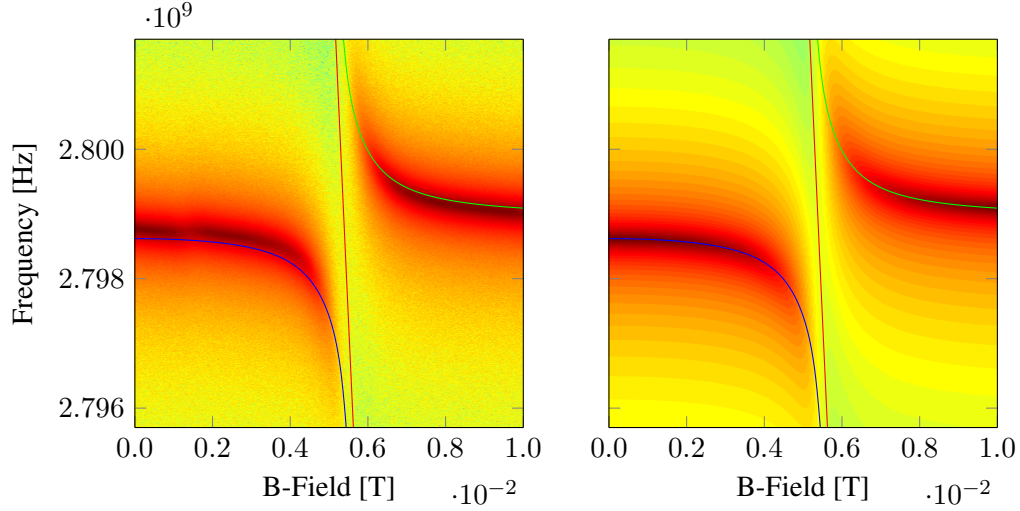


FIGURE 4.9: The calculated spectroscopic measurement for $(\phi = 2.46^\circ, \theta = 90.76^\circ)$ on the right is compared to the measurement on the left including the eigenvalues of the system. Deviations arise from the uncertain parameters due to weak coupling as well as a discrepancy produced by the C^{13} subensemble being on resonance for zero fields. The eigenvalues of the subensembles and the resonator are calculated with the system Hamiltonian in Eq. (2.27)

The single line passing through the avoided crossing are 3 eigenvalues overlapping, which are the antisymmetric sub radiant states of the system. The 4 eigenvalues ω_{s+1-4} for the transitions $|0\rangle \rightarrow |+1\rangle$ are not visible in the chosen frequency range. The eigenvalues deviate from the measurement especially prior to the avoided crossing, which could be due to the ^{13}C subensemble resonance. Mostly there is good agreement of the theory with the measurement even outside of the strong coupling regime. In the strong coupling regime γ could be measured exactly making it possible to optimize the theory. Overall the theoretical approach seems to be a stable option to check the measured parameters as well as making it an ideal precursor for longer measurements.

4.2 Coherent Coupling of Two Ensembles

This section deals with the coherent coupling between two spatially separated NV ensembles via the superconducting resonator. The aim for this measurement series is to show that two separated ensembles can transfer information coherently making them act as a single ensemble. Their separation could theoretically be utilized to address an isolated ensemble individually, for example by optical transitions induced by an additional optical fibre.

The resonator used is Nr.270 (see Section 3.4) which is a full wave type with two field maxima on which the diamonds are placed. Each diamond is twisted with a different angle with respect

to the resonator which leads to them having differing magnetic field behaviour. In Fig. 4.10 the setup is displayed, as well as a schematic of the diamonds with according subensembles. The twisting angles were roughly measured as 15.2° and -9.1° .

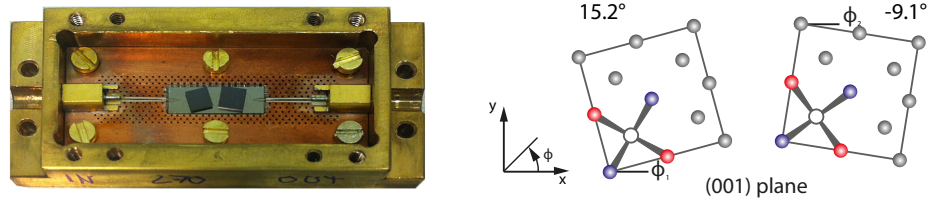


FIGURE 4.10: Double diamond schematic. On the left are both diamonds used in the experimental setup. On the right is the (001) plane projection of the diamonds each with their own in plane twist angle ϕ_1 and ϕ_2 . For $\phi = 48.1^\circ$ all blue subensembles of the spatially separated diamonds overlap which should produce a single enhanced avoided crossing in case of coherent coupling.

With these angles the two blue subensembles of Fig. 4.10b are maximally tuned for a magnetic field angle of 60.2° for the 15.2° -Diamond and 35.9° for the -9.1° -Diamond. Averaging these magnetic field angles leads to approximately 48.1° for which both pairs of blue subensembles are tuned identically. All four blue ensembles should produce an avoided crossing with a peak splitting increased by approximately $\sqrt{2}$ in comparison to a single diamond or two blue ensembles, assuming coherent coupling exists. To summarize, the first way of testing coherent coupling needs three measurements with the magnetic field angle ϕ at:

- $\phi = 15.2^\circ$: The 15.2° -Diamond is tuned weakly as all subensembles are 45° turned from the magnetic field. 2 subensembles of the -9.1° -Diamond experience stronger fields and produce the first avoided crossing with a coupling constant g_1 .
- $\phi = -9.1^\circ$: 2 subensembles of the 15.2° -Diamond produce the first avoided crossing with a coupling constant g_2 .
- $\phi = 48.1^\circ$: 4 subensembles, 2 from each diamond, produce the first avoided crossing with a coupling constant of $g_t = \left(\frac{g_2 + g_1}{2}\right) \cdot \sqrt{2}$, in case of coherent coupling.

The second way of testing is comparing measurements to the theoretical approach. Since the theory is based on collective coupling any discrepancy would proof the lack of it. The theory is therefore expanded to two different ensembles which leads to the T-Matrix dimension of 17×17 , 1 for the resonator and 8 per diamond. Required are the 6 parameters $(f_{res}, \frac{\kappa}{2})$ for the resonator, $(g_1, \frac{\gamma_1}{2})$ for the -9.1° -Diamond and $(g_2, \frac{\gamma_2}{2})$ for the 15.2° -Diamond. Furthermore the zero field parameters have to be measured which are assumed to be similar for both diamonds as they are produced by the same procedure.

The resonance frequency and resonator loss were measured at a temperature of 950 mK. Comparing this to the previous measurement it is expected that this is not the ideal temperature

and offsets should be anticipated. The resulting parameters are $f_{res} = 2.7491$ GHz and $\frac{\kappa}{2\pi} = 0.4$ MHz.

The dispersive measurement for the zero field parameters was made with a pump power of -50 dBm and probe power of -90 dBm, which is plotted in Fig. 4.11. The zero field parameters are measured to be $D = 2.877$ GHz and $E = 8$ MHz. For the remaining measurements the probe power of -70 dBm was applied.

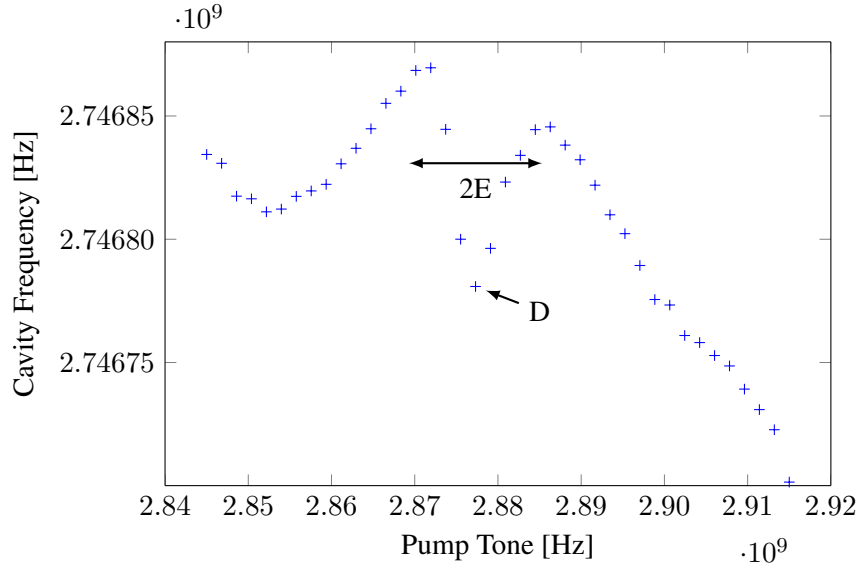


FIGURE 4.11: Dispersive measurement for zero field parameter of the double diamond experiment. The tilt originates from a temperature drift of 10 mK during the measurement, which is disregarded as the necessary parameters can be determined nevertheless. Due to the temperature drift instead of the cavity shift the current cavity frequency is plotted.

The next step is the θ angle correction to counteract any out of plane fields which additionally split the subensembles. As there is only a global magnetic field set by the Helmholtz coils the correction is not ideal since each diamond has a different offset. However as the diamond surface is polished the major factor for out of plane fields can be assumed to be a tilt of the resonator. In comparison to the Berkeley sample (Section 4.1) where a single correction was sufficient here a correction for arbitrary ϕ angles is needed for later measurements. Therefore the θ correction has to be made at the avoided crossing of two angles $\phi_1 = 48.1^\circ$ and $\phi_2 = (48.1 + 90)^\circ$, with other values interpolated. The field angle is set to ϕ_1 and ϕ_2 , with θ varied in the vicinity of 90° until the sharpest splitting is observed, for the angle θ_{corr} . This gives two correction values $\delta_{1,2} = 90 - \theta_{corr1,2}$ for ϕ_1 and ϕ_2 . For arbitrary ϕ the corrected angle θ is calculated as $\theta_{corr} = \arccos(\cos(\phi - 48.1^\circ \frac{\pi}{180^\circ}) \cdot \sin(\delta_1) + \sin(\phi - 138.1^\circ \frac{\pi}{180^\circ}) \cdot \sin(\delta_2))$. In Fig. 4.12 the corresponding angles are depicted.

The spectroscopic measurements with the fixed angles $\phi = (15.2^\circ, -9.1^\circ, 48.1^\circ)$ have two purposes. Firstly they are the first verification of coherent coupling via the \sqrt{N} increase of the coupling constant. Secondly they provide the necessary parameters for the theoretical approach.

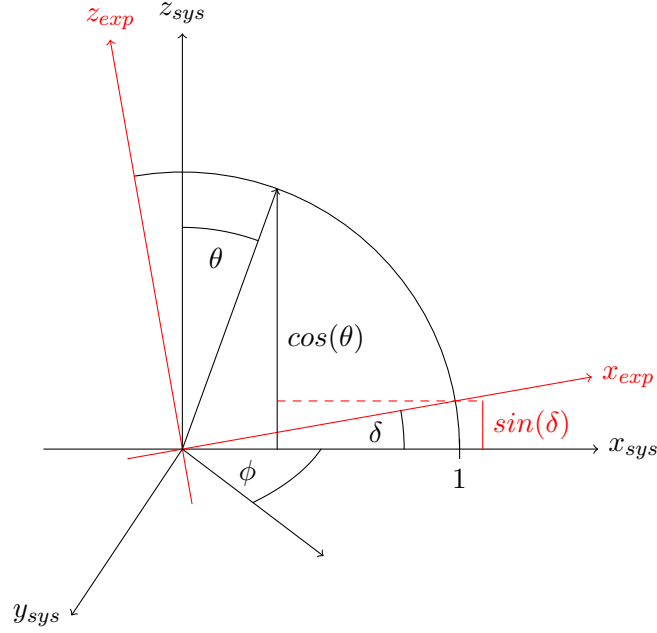


FIGURE 4.12: Theta correction schematic. With two diamonds arbitrary ϕ directions have to be measured to overlap different subensembles to obtain all necessary parameters. Therefore, for two perpendicular in plane directions a correction value δ has to be found to calculate θ_{corr} for every possible in plane angle.

The applied measurement angles were $\phi = 79^\circ$, which is equivalent to -9.1° , and $\phi = 16^\circ$. In Fig. 4.13 the spectroscopic results are plotted on the left side and the according avoided crossings on the right side.

The obtained values for the measurement with $\phi = 16^\circ$ are $\left(\frac{\Omega_1}{2\pi}, \frac{\Gamma_1}{2\pi}\right) = (11.2, 6.0)\text{MHz}$ which gives the calculated parameters $\left(\frac{g_1}{2\pi}, \frac{\gamma_1}{2\pi}\right) = (6.3, 11.5)\text{MHz}$. For the magnetic field angle $\phi = 79^\circ$ the values are $\left(\frac{\Omega_2}{2\pi}, \frac{\Gamma_2}{2\pi}\right) = (14.8, 3.4)\text{MHz}$ and accordingly $\left(\frac{g_2}{2\pi}, \frac{\gamma_2}{2\pi}\right) = (7.7, 6.4)\text{MHz}$. Especially for the -9.1° -Diamond the full form of the vacuum Rabi splitting has to be used as the approximation differs by 10 %. Both splittings are produced by 2 subensembles so the coupling constants have to be multiplied by $\frac{1}{\sqrt{2}}$ for a single subensemble.

For the magnetic field angle $\phi = 48.1^\circ$, as seen in Fig. 4.14, the obtained values are $\left(\frac{\Omega_t}{2\pi}, \frac{\Gamma_t}{2\pi}\right) = (19.1, 3.2)\text{MHz}$ with $\left(\frac{g_t}{2\pi}, \frac{\gamma_t}{2\pi}\right) = (9.7, 6.0)\text{MHz}$. The averaged value of both diamonds is $\frac{g_1+g_2}{2} = 2\pi \cdot 7.0\text{MHz}$, by multiplying this with $\sqrt{2}$ for coherent coupling the value 9.9 MHz is obtained. This value agrees well with the measured $g_t = 9.7\text{MHz}$ indicating that coherent coupling between the diamond is present.

To summarize, the theoretical approach is composed of the parameters $\omega_c = 2\pi \cdot 2.7491\text{GHz}$ and $(g_1, g_2, \frac{\kappa}{2}, \frac{\gamma_1}{2}, \frac{\gamma_2}{2}) = 2\pi \cdot (\frac{6.3}{\sqrt{2}}, \frac{7.7}{\sqrt{2}}, 0.2, 5.8, 3.2)\text{MHz}$. The transmission amplitude at the avoided crossing is -74dB . Applying this value to the calculation leads to an offset of -3dB or factor $\frac{1}{2}$ in the transmission. This offset may be due to the duplication of the ensemble in the

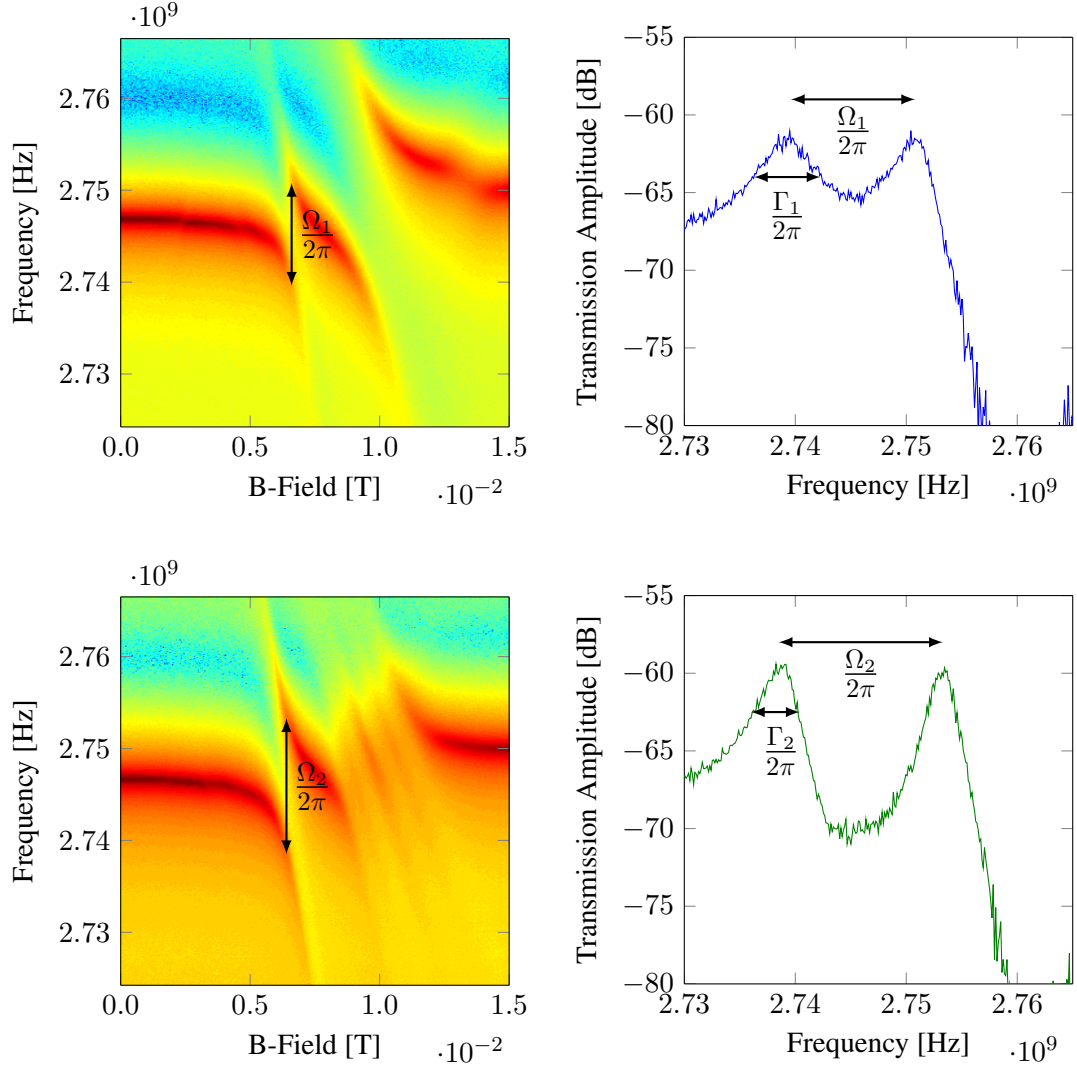


FIGURE 4.13: Spectroscopic transmission measurements of individual diamonds at $\phi = 16^\circ$ (upper), 79° (lower). At these angles all 4 subensembles of a single diamond are equally weakly tuned and in turn 2 subensembles of the other diamond are tuned strongly. Therefore, the first avoided crossing is produced by 2 subensembles of one diamond and the second larger avoided crossing by all 4 subensembles of the other diamond. For the $\phi = 79^\circ$ (lower) measurement the larger avoided crossing shows effects of out of plane fields. This can not be removed as each individual diamond would need a different θ correction.

theory, however, the origin has yet to be determined. To counteract the offset the transmission at the avoided crossing for overlapping diamonds is taken as $|t(\omega = \omega_c = \omega_{s_{1-4}})| = 10^{-77/10}$ with the average photon number $n_{avg} = 0.0085$. The zero field parameters of the spin ensemble are $D = 2.877$ GHz and $E = 8$ MHz.

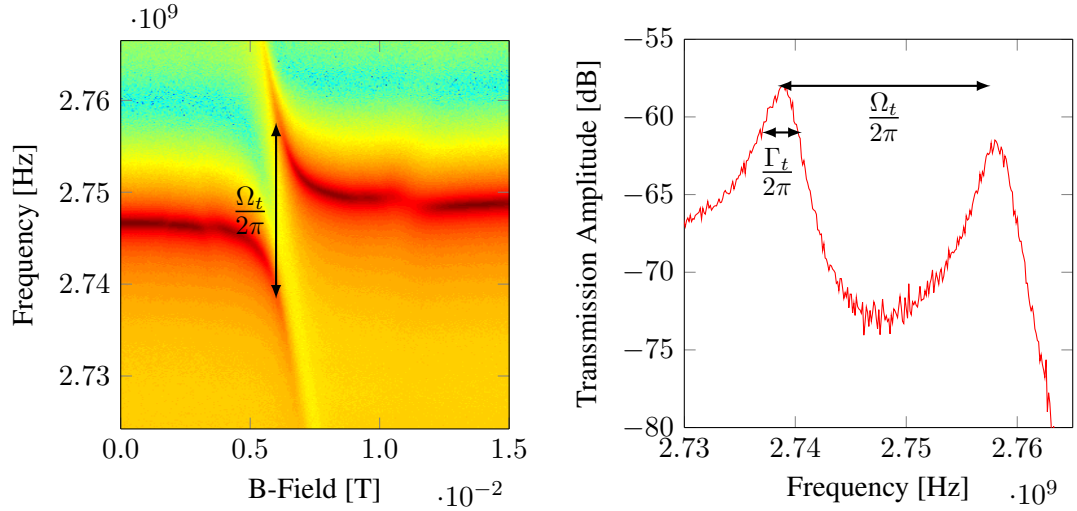


FIGURE 4.14: Spectroscopic transmission measurements of double diamond at $\phi = 48.1^\circ$. At this angle two subensembles of each diamond overlap to produce the single avoided seen in the figure. The splitting of Ω_t , produced by 4 subensembles, should be enhanced by $\sqrt{2}$ in comparison to $\Omega_{1/2}$, produced by 2 subensembles, in case of coherent coupling.

The Fano resonance is fitted at zero field where the transmission spectrum only is influenced by the resonator. The fit results are $A_f = 0.03$ and $\phi_f = 255^\circ \cdot \frac{\pi}{180^\circ}$. In Fig. 4.15 the calculated transmission with and without the Fano term is compared to the measurement.

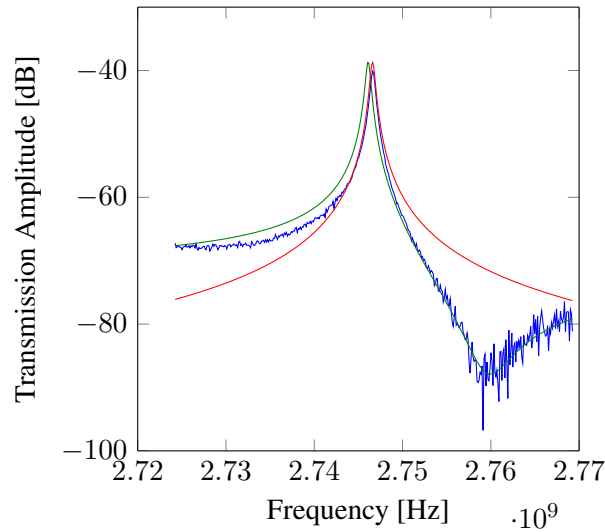


FIGURE 4.15: Transmission spectrum for zero magnetic field. The measurement is plotted in blue, the theory is in red without Fano resonance and in green with Fano resonance. While the calculation including the Fano resonance shows overall better agreement it shifts the initial resonance frequency. This leads to the conclusion that the fitted resonance frequency is not independent of the Fano resonance. Any calculation using this resonance frequency will deviate for measurements with strong Fano resonances.

For the comparison to the theory the measurement is changed with a different mode of operation for the magnetic field. Instead of increasing the field amplitude of the field for fixed angles the amplitude is fixed and ϕ is changed with corresponding corrected $\theta = 90^\circ$. The amplitude is set near a value for which an avoided crossing occurs at 48.1° . The magnetic field amplitude is chosen to be $|B| = 6.2$ mT for the following measurements and calculations. The advantage of this operation mode is that the evolution of coupling with increasing overlap of the subensembles can be observed. The possible calculated eigenvalue behaviour is illustrated in Fig. 4.16.

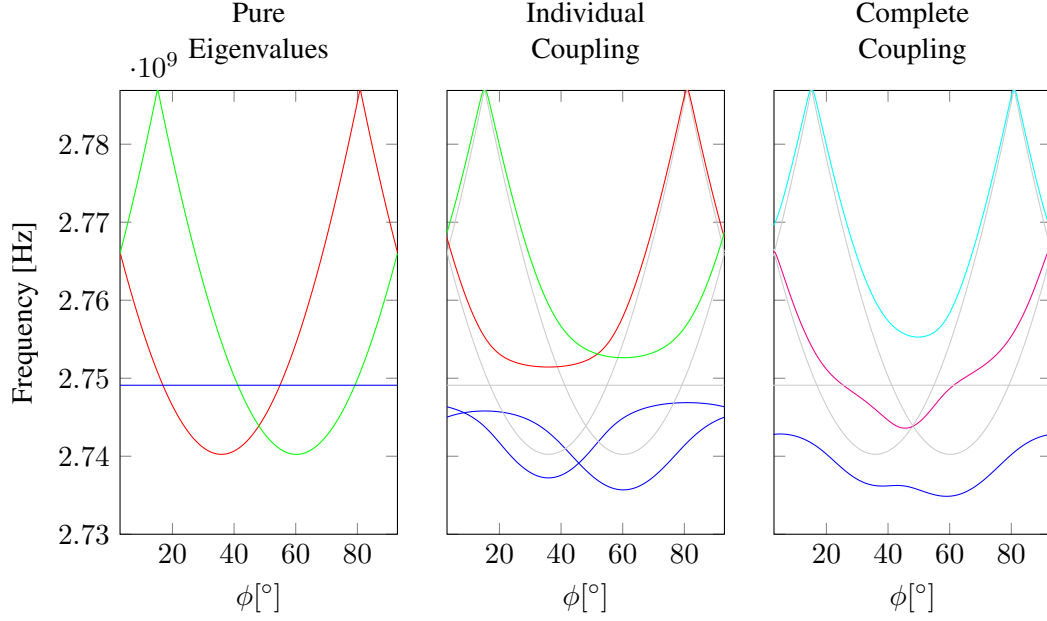


FIGURE 4.16: Possible eigenvalue behaviour for $|B| = 6.2$ mT depending on the coupling between the ensembles and the resonator. The eigenvalues are blue for the resonator, red for the -9.1° -Diamond and green for the 15.2° -Diamond. All uncoupled eigenvalues are depicted in grey. In the left plot the pure eigenvalues of the system are plotted without any interaction between resonator and the diamonds. In the middle the individual coupling equates to two systems each with a single distinct diamond interacting with a resonator. In the last plot for complete coupling each diamond interacts with the same resonator and therefore with each other. For coherent coupling the upper eigenvalue at 48.1° is the fully symmetric Dicke state and is expected to be super radiant. Whereas the middle eigenvalue state should be sub radiant as it is asymmetric.

Finally the transmission spectroscopy versus ϕ is shown in Fig. 4.17a. Alongside it are transmission with coherent coupling Fig. 4.17b and incoherent coupling Fig. 4.17c for comparison. For the incoherent coupling plot the interaction between each diamond and the resonator is considered to be isolated, effectively producing two resonator systems with their own resonator eigenvalue. The complex transmissions of each system with one resonator and one diamond are averaged with $t = t_{-9.1^\circ} + t_{15.2^\circ}$. The comparison shows an agreement for the measurement with coherent coupling.

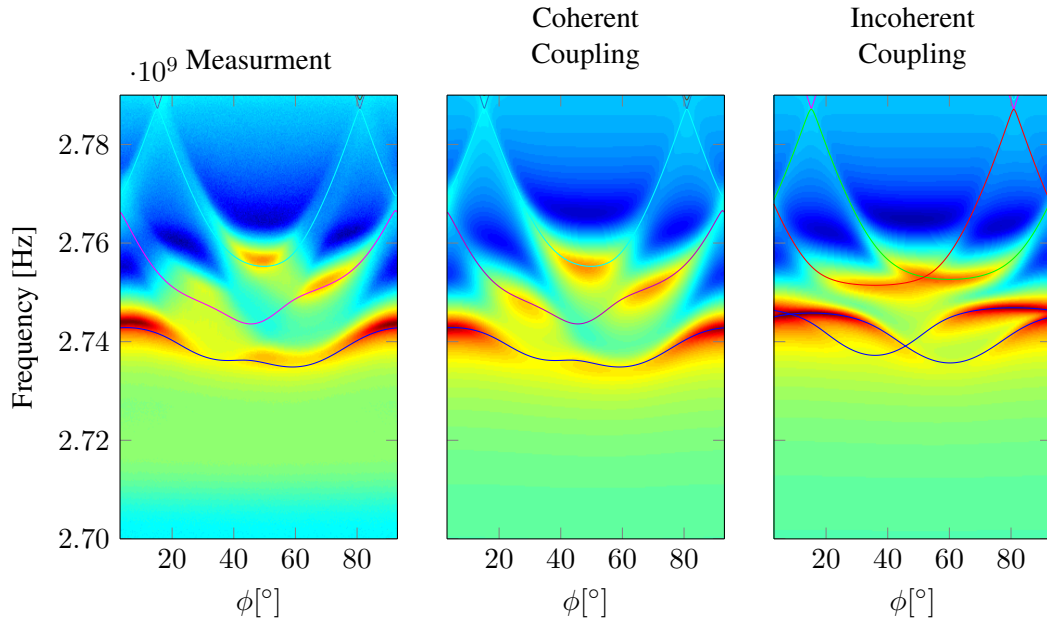


FIGURE 4.17: Spectroscopic transmission measurements versus ϕ for $|B| = 6.2$ mT. All figures are plotted in the same colour range. The measurement shows the same distinct features as the coherent coupling calculation. At 48.1° the transmission for 2.75 GHz vanishes indicating the sub radiant state. For 2.76 GHz the transmission has a high amplitude even though it is further off resonance than other transmissions. This corresponds to a super-radiant state. In comparison the incoherent coupling calculation shows different behaviour.

In summary the system shows clear indication of coherent coupling between the two diamonds for both methods of proof. Firstly, the coupling does increase by a factor of approximately $\sqrt{2}$ with the transition overlap of both diamonds. Secondly, the development of a super and sub radiant state can be seen during the overlap. Therefore, each diamond can be considered to be a subensemble of a bigger ensemble comprised of both diamonds.

Chapter 5

Outlook

After showing coherent information transfer between the quantum storage systems via the quantum bus, there are different ways to advance the experiment. One way is to add superconducting qubits with Josephson junctions to the system for information processing. Another way is to implement a fibre above the diamonds to manipulate them with optical transitions. The diamonds used in the experiment show a strong optical density after producing the NV defects due to the applied neutron irradiation. Consequently the fibre has to apply high power for light to reach the lowest plane of the diamond, where the main interaction with the photons in the resonator takes place. This would lead to heating of the whole system which is problematic with the limited cooling energy of the ADR. Using electron irradiation to produce the NV defects does not influence the transparency of the diamond but in return lower coupling strengths are achieved. Another option is to change the type of spin ensemble used. A promising substitute to NV defects are nanomagnets which are shortly discussed in the following section.

5.1 Alternative Spin Ensemble: Nanomagnets

Nanomagnets consist of a high spin magnetic core which is surrounded by an organic ligand shell [16, 22]. Typically rare earth elements are used as the magnetic core. By choosing elements without a nuclear spin the coherence time can be improved. By chemical design the intrinsic parameters of the nanomagnets like spin and magnetic anisotropy can be changed making them more versatile than other qubit systems. They typically show high total spin values which leads to increased coupling to the magnetic field and theoretically complex information can be written inside the formed multiplets [1]. Crystalline nanomagnets have a high density of magnetic cores, increasing the coupling furthermore. Optionally, the density can be altered by dilution, where the magnetic core is replaced by a non magnetic one.

There are two types of nanomagnets depending on the magnetic core, single molecule magnets (SMM) and single ion magnets (SIM). SMM are problematic to implement in the current system setup as they have a large magnetic anisotropy barrier (D above 100 GHz) which would require either high frequencies or strong external fields. Furthermore the controlled fabrication of molecule cores is harder than for single ions. Therefore the main interest lies in SIM nanomagnets for the current experimental setup.

First tests were made with nanomagnets provided by the group of Fernando Luis in Saragossa. The magnetic core consists of Gd^{3+} which has a $4f^7$ electronic configuration resulting in an electronic ground state with $L = 0$ and $S = \frac{7}{2}$ with the gyromagnetic ratio $g_j \approx 2$ [24, 25]. This leads to a magnetic moment $\vec{\mu} = g_j \mu_B \vec{J} \approx \vec{S} \cdot 28 \frac{\text{MHz}}{\text{mT}}$. In the diluted variation the magnetic core is replaced by a Y^{3+} . The core is coordinated to a polyoxometalate (POM) molecule of the form $[\text{Gd}(\text{P}_5\text{W}_{30}\text{O}_{110})]^{12-}$. In the experiment used is the potassium salt of the POM, $\text{K}_{12}(\text{Gd}(\text{P}_5\text{W}_{30}\text{O}_{110}) \cdot 54\text{H}_2\text{O})$, shortened to GdW_{30} . Even though L is 0 for the ground state, GdW_{30} shows weak anisotropy at low temperatures created by coulomb interaction of near neighbour ions. The crystal field induces mixing of the ground state multiplet with excited state multiplets, for which L can be nonzero. The near neighbour interaction is influenced by the structure of the local coordination sphere dictated by the used POM structure. GdW_{30} has a large intermolecular distance and therefore weak intermolecular dipolar interaction even in undiluted samples. Below a temperature $T < 200 \text{ mK}$ spin lattice relaxation is mainly created by quantum tunnelling.

Using the same form of the spin Hamiltonian as in Eq. (2.20) the two zero field parameters D and E were estimated by fitting the absorption spectrum of a broadband electron paramagnetic resonance (EPR) [25]. Measurements were made with a powder sample at temperatures of 10 K and 1.7 K with $f = 25 \text{ GHz}$ in the magnetic field range of 0.4 T to 1.4 T. The best fitting results were received with $D = 1.1877 \text{ GHz}$ and $E = 0.3959 \text{ GHz}$. Unfortunately these measurements were made with far higher temperatures and magnetic fields than in the experimental setup used for this work. The hyperfine term produced by interaction with the nuclear spin I of the ion is not included in the spin Hamiltonian. Naturally occurring gadolinium consists of 6 isotopes for which 2 (^{155}Gd , ^{157}Gd) have a nuclear spin $I \neq 0$. They both have a natural abundance of about 15 % which can produce more obvious deviations than for NV diamonds.

With $D > 0$ and $E = 0$ the mainly populated levels for low temperatures are those with $m_s = \pm \frac{1}{2}$ for the quantisation axis in z direction. With the not negligible E parameter significant level mixing occurs which produces ground states which are not purely $m_s = \pm \frac{1}{2}$. These mixed states dominate in the whole range of the magnetic field applicable in the system setup. Therefore the Zeeman tuning of $\approx 28 \frac{\text{MHz}}{\text{mT}}$ is not valid anymore.

The Matlab library EasySpin [33] was used to calculate the eigenvalues and transition frequencies of the spin system in Fig. 5.1.

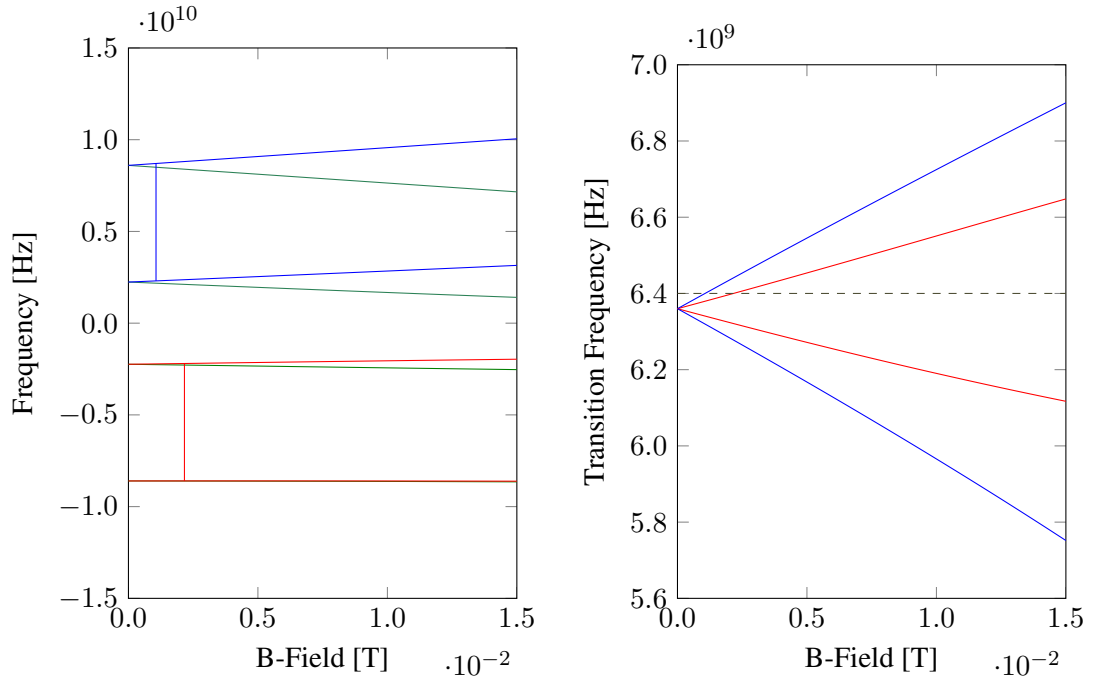


FIGURE 5.1: Eigenfrequencies and transition frequencies for GdW_{30} . Due to the low temperatures the upper levels are mostly unoccupied and the blue transitions are negligible. The black dashed line is the resonator frequency of 6.4 GHz which also corresponds to the transition marked in the level frequencies.

Due to the positive D there is a disadvantage as the ground state transition dominated by $m_s = \pm\frac{1}{2} \rightarrow \pm\frac{3}{2}$ is not tuned as strongly, $\approx 17 \frac{\text{MHz}}{\text{mT}}$, as the excited state transition dominated by $m_s = \pm\frac{5}{2} \rightarrow \pm\frac{7}{2}$, $\approx 40 \frac{\text{MHz}}{\text{mT}}$. This reduces the tuning window quite a lot which makes the uncertainty of the zero field parameters even more problematic. The ground state transition occurs at 2 mT for 6.4 GHz between the states $|g\rangle = -0.8|\frac{1}{2}\rangle + 0.5|-\frac{3}{2}\rangle + 0.2|\frac{5}{2}\rangle - 0.1|-\frac{7}{2}\rangle$ and $|e\rangle = 0.8|\frac{3}{2}\rangle + 0.4|-\frac{1}{2}\rangle - 0.3|-\frac{5}{2}\rangle - 0.1|\frac{7}{2}\rangle$. With the used temperature of 70 mK in the experiment the ground state has a polarization degree of 97 % for the transition frequency of approximately 6.35 GHz at zero field.

Measurements of GdW_{30} were made with a half wave resonator (Nr.331 at 6.2 GHz) and TLER (Nr.521 at 6.4 GHz). For both resonators the quality factor Q was reduced by more than a factor 10 after loading of the nanomagnet crystal. However in comparison to the loading of the NV diamond, where resonance frequency shifts in the order of 100 MHz are observed, for nanomagnets at most shifts in the order of 10 MHz were produced.

In Fig. 5.2 the transmission spectrum measured with the half wave resonator for two different temperatures is shown. Whereas Q is reduced from 2000 to 400 the resonance frequency barely changes. This shows that the polarized spin system does influence the resonator, however, mainly with much higher losses than NV diamonds without any apparent dispersive shift.

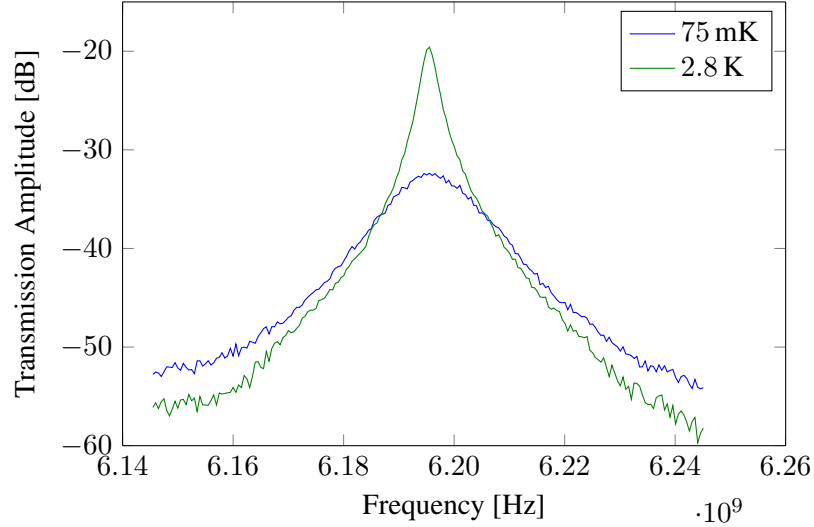


FIGURE 5.2: Nanomagnet transmission spectrum for different temperatures. While the losses become apparent with increased polarization of the spins the resonance frequency does barely shift from the initial value. This can be interpreted as the spins not coherently increasing the coupling strength and therefore the dispersive shift while their individual losses are still present.

Neither strong nor weak coupling was observed in the transmission spectrum in the whole magnetic field range. This could be a simple problem of the wrong zero field parameters which could shift the transmission outside of the tuning window. Using resonators with different resonance frequencies the correct transition window could be found.

However a far more problematic aspect are the salt crystal properties of the nanomagnets. Stored in solution they keep their crystalline form but as soon as they come in contact with air they start to lose their transparency due to water loss and become fragile. In Fig. 5.3 the GdW_{30} crystal can be seen before, recently removed from the solution, and after the experiment. At the beginning the crystal still has some transparency while at the end the crystal would break apart by small vibrations. Assuming the individual POM molecules are kept intact during the experiment the problem with crystal order remains. The loss of crystal order would result in different magnetic fields for each individual POM molecule. In this experimental setup the ensemble property of increased coupling ($g_{\text{eff}} = \sqrt{N}g$) is necessary for a signal above the noise floor. This could explain why Q decreases, as it is independent of spin orientation, while no dispersive shift is seen, since it is proportional to g_{eff}^2 . Therefore, the absence of any coupling may be due to the low coupling strength while the zero field parameters are correct. Since it is impossible to distinguish the source of the problem further measurements with more averages are pointless.

Another problematic aspect is the contact area of the crystals with the resonators. In comparison to the smoothed diamonds the nanomagnets have a rough surface. This leads to additional strong reduction of the coupling strength. In theory using TLER this should be less of a problem as the necessary contact area is much smaller, however, in the experiment missing the resonator altogether was very likely. There were attempts to decrease the roughness of the crystals by either

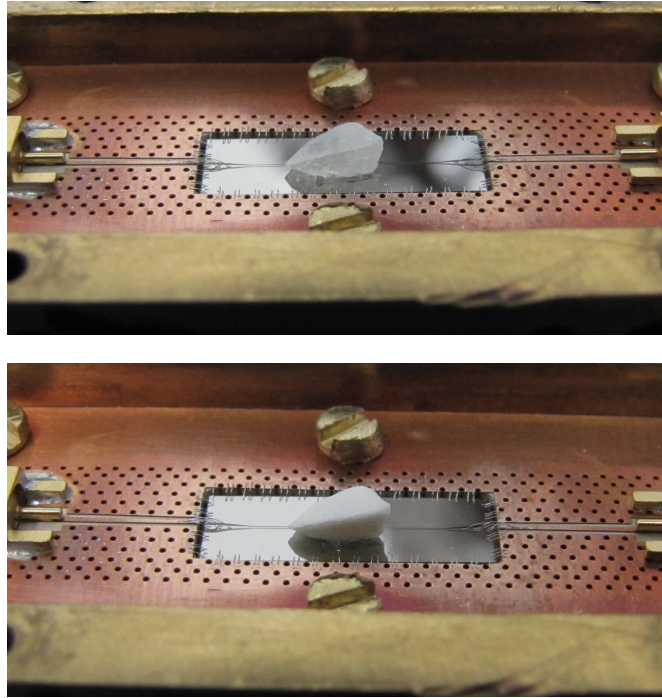


FIGURE 5.3: Nanomagnet before (above) and after (below) experiment. The nanomagnet losses most of its crystal structure during the experiment. This could be the reason for no apparent dispersive shift, as the individual spins do not have the same orientation towards the field in the resonator and no enhancement of the coupling strength by \sqrt{N} occurs.

putting the nanomagnets in an epoxy glue for support and grinding the surface or growing the crystals directly on the resonator. Although the grinding produced smoother surfaces no obvious differences in the measurement were observed. As there is no way to check the condition of the crystal inside the glue it is inconclusive if this method could be used in later measurements. The crystals can be dissolved in water and reform by increasing the concentration of the nanomagnets. Growing the crystals on the resonator was possible, however, the control of the growth position is difficult. Once the resonator was removed from the solution the same problem with water loss occurred.

In conclusion, whereas the potential of spin systems based on nanomagnets is high, there is no clear indication of feasibility. The major problem which has to be solved first is the production of consistent stable crystals which can be measured in cryogenic temperatures. After the crystal order can be guaranteed further attempts to locate the transition frequencies can be made. At this point it is not possible to conclude if the zero field parameters can be extrapolated down to lower temperatures and fields.

Acknowledgements

The time I spent in the Atomchip group was a great joy and an instructional experience which would not have been possible without the people working there.

I want to express my thanks to,

Jörg Schmiedmayer, for the opportunity to work in his group and providing us the framework for our experiment.

Johannes Majer, for his continuous and more importantly patient supervision during my work. I can not count the number of times I had to revise my understanding of the experiment after our discussions.

Thomas Astner for the cooperation during the experiments, the discussions about potentially stupid questions and the many proof readings of my thesis.

Stefan Putz, Andreas Angerer and Ralph Glattauer for the sharing of ideas, lab and in addition Andreas for his proof reading of my thesis.

The people who provided the basis for our experiment, in particular Robert Amsüss and Christian Koller.

The whole Atomchip group which always felt welcoming, even during the crowded lunch hours.

My friends providing the necessary distraction from time to time.

My whole family, especially my parents and my brother who support me since I can remember.

Bibliography

1. M. Affronte. Molecular nanomagnets for information technologies. *J. Mater. Chem.*, 19 (12):1731–1737, 2009. ISSN 0959-9428. doi: 10.1039/B809251F.
2. S. Agarwal, S. M. H. Rafsanjani, and J. H. Eberly. Tavis-Cummings model beyond the rotating wave approximation: Quasidegenerate qubits. *Physical Review A - Atomic, Molecular, and Optical Physics*, 85(4):324–328, 2012. ISSN 10502947. doi: 10.1103/PhysRevA.85.043815.
3. R. Amsüss. *Strong coupling of an NV- spin ensemble to a superconducting resonator*. PhD thesis, 2013.
4. R. Amsüss, C. Koller, T. Nöbauer, S. Putz, S. Rotter, K. Sandner, S. Schneider, M. Schramböck, G. Steinhauser, H. Ritsch, J. Schmiedmayer, and J. Majer. Cavity QED with Magnetically Coupled Collective Spin States. *Physical Review Letters*, 107(6):060502, Aug. 2011. ISSN 0031-9007. doi: 10.1103/PhysRevLett.107.060502.
5. G. Bensky, R. Amsüss, J. Majer, D. Petrosyan, J. Schmiedmayer, and G. Kurizki. Controlling quantum information processing in hybrid systems on chips. *Quantum Information Processing*, 10(6):1037–1060, 2011. ISSN 15700755. doi: 10.1007/s11128-011-0302-6.
6. R. H. Dicke. Coherence in spontaneous radiation processes. *Physical Review*, 93(1):99–110, 1954. ISSN 0031899X. doi: 10.1103/PhysRev.93.99.
7. I. Diniz, S. Portolan, R. Ferreira, J. M. Gérard, P. Bertet, and A. Auffèves. Strongly coupling a cavity to inhomogeneous ensembles of emitters: Potential for long-lived solid-state quantum memories. *Physical Review A*, 84(6):063810, Dec. 2011. ISSN 1050-2947. doi: 10.1103/PhysRevA.84.063810.
8. D. P. Divincenzo. Topics in Quantum Computers. *Mesoscopic Electron Transport*, pages 657–677, 1997. doi: 10.1007/978-94-015-8839-3_18.
9. M. W. Doherty, F. Dolde, H. Fedder, F. Jelezko, J. Wrachtrup, N. B. Manson, and L. C. L. Hollenberg. Theory of the ground-state spin of the NV - center in diamond. *Physical Review B - Condensed Matter and Materials Physics*, 85(20):205203, May 2012. ISSN 10980121. doi: 10.1103/PhysRevB.85.205203.

10. M. W. Doherty, J. Michl, F. Dolde, I. Jakobi, P. Neumann, N. B. Manson, and J. Wrachtrup. Measuring the defect structure orientation of a single NV- centre in diamond. *New Journal of Physics*, 16, 2014. ISSN 13672630. doi: 10.1088/1367-2630/16/6/063067.
11. F. Dyson. The S Matrix in Quantum Electrodynamics. *Physical Review*, 75(11):1736–1755, 1949. ISSN 0031-899X. doi: 10.1103/PhysRev.75.1736.
12. D. Garcia. Robust smoothing of gridded data in one and higher dimensions with missing values. *Computational Statistics and Data Analysis*, 54(4):1167–1178, 2010. ISSN 01679473. doi: 10.1016/j.csda.2009.09.020.
13. D. Garcia. A fast all-in-one method for automated post-processing of PIV data. *Experiments in Fluids*, 50(5):1247–1259, 2011. ISSN 07234864. doi: 10.1007/s00348-010-0985-y.
14. C. Gardiner and M. Collett. Input and output in damped quantum systems: Quantum stochastic differential equations and the master equation. *Physical Review A*, 31(6):3761–3774, June 1985. ISSN 0556-2791. doi: 10.1103/PhysRevA.31.3761.
15. B. M. Garraway. The Dicke model in quantum optics: Dicke model revisited. *Philosophical transactions. Series A, Mathematical, physical, and engineering sciences*, 369(1939):1137–1155, 2011. ISSN 1364-503X. doi: 10.1098/rsta.2010.0333.
16. D. Gatteschi, R. Sessoli, and J. Villain. *Molecular Nanomagnets*. 2006. ISBN 9780198567530. doi: 10.1093/acprof.
17. M. Göppl, A. Fragner, M. Baur, R. Bianchetti, S. Filipp, J. M. Fink, P. J. Leek, G. Puebla, L. Steffen, and A. Wallraff. Coplanar waveguide resonators for circuit quantum electrodynamics. *Journal of Applied Physics*, 104(11), 2008. ISSN 00218979. doi: 10.1063/1.3010859.
18. K. Henschel, J. Majer, J. Schmiedmayer, and H. Ritsch. Cavity QED with an ultracold ensemble on a chip: Prospects for strong magnetic coupling at finite temperatures. *Physical Review A - Atomic, Molecular, and Optical Physics*, 82(3):1–16, 2010. ISSN 10502947. doi: 10.1103/PhysRevA.82.033810.
19. T. Holstein and H. Primakoff. Field dependence of the intrinsic domain magnetization of a ferromagnet. *Physical Review*, 58(12):1098–1113, 1940. ISSN 0031899X. doi: 10.1103/PhysRev.58.1098.
20. E. Jaynes and F. Cummings. Comparison of quantum and semiclassical radiation theories with application to the beam maser. *Proceedings of the IEEE*, 51(1), 1963. ISSN 0018-9219. doi: 10.1109/PROC.1963.1664.
21. F. Jelezko and J. Wrachtrup. Single defect centres in diamond: A review, Oct. 2006. ISSN 18626300.

22. M. Jenkins, T. Hümmer, M. J. Martínez-Pérez, J. García-Ripoll, D. Zueco, and F. Luis. Coupling single-molecule magnets to quantum circuits. *New Journal of Physics*, 15(9): 095007, Sept. 2013. ISSN 1367-2630. doi: 10.1088/1367-2630/15/9/095007.
23. Z. Kurucz, J. H. Wesenberg, and K. Mølmer. Spectroscopic properties of inhomogeneously broadened spin ensembles in a cavity. *Physical Review A - Atomic, Molecular, and Optical Physics*, 83(5):053852, May 2011. ISSN 10502947. doi: 10.1103/PhysRevA.83.053852.
24. F. Li and X. Duan. Applications of Layered Double Hydroxides. *Structure and Bonding*, 119(September 2005):193–223, 2006. ISSN 00815993. doi: 10.1007/430.
25. M. J. Martínez-Pérez, S. Cardona-Serra, C. Schlegel, F. Moro, P. J. Alonso, H. Prima-García, J. M. Clemente-Juan, M. Evangelisti, A. Gaita-Ariño, J. Sesé, J. van Slageren, E. Coronado, and F. Luis. Gd-Based Single-Ion Magnets with Tunable Magnetic Anisotropy: Molecular Design of Spin Qubits. *Physical Review Letters*, 108(24):247213, June 2012. ISSN 0031-9007. doi: 10.1103/PhysRevLett.108.247213.
26. P. C. Maurer, G. Kucsko, C. Latta, L. Jiang, N. Y. Yao, S. D. Bennett, F. Pastawski, D. Hunger, N. Chisholm, M. Markham, D. J. Twitchen, J. I. Cirac, and M. D. Lukin. Room-Temperature Quantum Bit Memory Exceeding One Second. *Science*, 336(6086): 1283–1286, 2012. ISSN 0036-8075. doi: 10.1126/science.1220513.
27. J. Michl, T. Teraji, S. Zaiser, I. Jakobi, G. Waldherr, F. Dolde, P. Neumann, M. W. Doherty, N. B. Manson, J. Isoya, and J. Wrachtrup. Perfect alignment and preferential orientation of nitrogen-vacancy centers during chemical vapor deposition diamond growth on (111) surfaces. *Applied Physics Letters*, 104(10):6, 2014. ISSN 00036951. doi: 10.1063/1.4868128.
28. T. Niemczyk, F. Deppe, H. Huebl, E. P. Menzel, F. Hocke, M. J. Schwarz, J. J. Garcia-Ripoll, D. Zueco, T. Hümmer, E. Solano, A. Marx, and R. Gross. Beyond the Jaynes-Cummings model: circuit QED in the ultrastrong coupling regime. *Nature Physics*, 6(10): 5, 2010. ISSN 1745-2473. doi: 10.1038/nphys1730.
29. D. Pozar. *Microwave Engineering*. John Wiley & Sons, 4th edition, 2011. ISBN 9780470631553.
30. I. I. Rabi. On the process of space quantization. *Physical Review*, 49(4):324–328, 1936. ISSN 0031899X. doi: 10.1103/PhysRev.49.324.
31. P. W. Shor. Polynomial-Time Algorithms for Prime Factorization and Discrete Logarithms on a Quantum Computer. *SIAM J. Comput.*, 26(5):1484–1509, 1997. ISSN 0097-5397. doi: 10.1137/S0097539795293172.

32. R. N. Simons. *Coplanar Waveguide Circuits , Components , and Systems*, volume 7. John Wiley & Sons, 2001. ISBN 0471161217.
33. S. Stoll and A. Schweiger. EasySpin, a comprehensive software package for spectral simulation and analysis in EPR. *Journal of Magnetic Resonance*, 178(1):42–55, 2006. ISSN 10907807. doi: 10.1016/j.jmr.2005.08.013.
34. M. Tavis and F. W. Cummings. Exact Solution for an N -Molecule—Radiation-Field Hamiltonian. *Physical Review*, 170(2):379–384, June 1968. ISSN 0031-899X. doi: 10.1103/PhysRev.170.379.
35. M. Travis and F. W. Cummings. Approximate solutions for an N-molecule-radiation-field Hamiltonian. *Physical Review*, 188(2):692–695, Dec. 1969. ISSN 0031899X. doi: 10.1103/PhysRev.188.692.
36. J. R. Weber, W. F. Koehl, J. B. Varley, A. Janotti, B. B. Buckley, C. G. Van de Walle, and D. D. Awschalom. Quantum computing with defects. *Proceedings of the National Academy of Sciences of the United States of America*, 107(19):8513–8518, 2010. ISSN 1091-6490. doi: 10.1073/pnas.1003052107.
37. J. A. Weil and J. R. Bolton. *Electron Paramagnetic Resonance*. 2006. ISBN 9780470084984. doi: 10.1002/0470084987.
38. Z.-L. Xiang, S. Ashhab, J. You, and F. Nori. Hybrid quantum circuits: Superconducting circuits interacting with other quantum systems. *Reviews of Modern Physics*, 85(June): 623–653, 2013. ISSN 0034-6861. doi: 10.1103/RevModPhys.85.623.